Spring 5-16-2018

A New Finite Difference Time Domain Method to Solve Maxwell's Equations

Timothy P. Meagher
Portland State University

A New Finite Difference Time Domain Method to Solve Maxwell's Equations

by

Timothy P. Meagher

A dissertation submitted in partial fulfillment of the
requirements for the degree of

Doctor of Philosophy
in
Mathematical Sciences

Dissertation Committee:
Bin Jiang, Chair
Dacian Daescu
Andres La Rosa
James Morris

Portland State University
2018

Abstract

We have constructed a new finite-difference time-domain (FDTD) method in this project. Our new algorithm focuses on the most important and more challenging transverse electric (TE) case. In this case, the electric field is discontinuous across the interface between different dielectric media. We use an electric permittivity ϵ that stays as a constant in each medium, and magnetic permittivity that is constant in the whole domain. To handle the interface between different media, we introduce new effective permittivities that incorporates electromagnetic fields boundary conditions. That is, across the interface between two different media, the tangential component $\mathbf{E}_\tau(x, y)$ of the electric field and the normal component $\mathbf{D}_n(x, y)$ of the electric displacement are continuous. Meanwhile, the magnetic field $\mathbf{H}(x, y)$ stays as continuous in the whole domain. Our new algorithm is built based upon the integral version of the Maxwell's equations as well as the above continuity conditions. The theoretical analysis shows that the new algorithm can reach second-order convergence $\mathcal{O}(\Delta x^2)$ with mesh size Δx. The subsequent numerical results demonstrate this algorithm is very stable and its convergence order can reach very close to second order, considering accumulation of some unexpected numerical approximation and truncation errors. In fact, our algorithm has clearly demonstrated significant improvement over all related FDTD methods using effective permittivities reported in the literature. Therefore, our new algorithm turns out to be the most effective and stable FDTD method to solve Maxwell's equations involving multiple media.

Dedication

This dissertation is dedicated to my mother, KarryLu Carpenter, who has always been there for me and encouraged me to grow, truly one of the best mothers out there.

Acknowledgments

I would like to thank all of my professors that help me along the way. Many of them had a great influence on me. The first name I want to mention is Dr. John Caughman, who helped me with finishing my master degree and getting into the Ph.D. program. His help and kindness means so much to me. Another name in need of mentioning is Dr. James C. Selser from University of Nevada at Las Vegas, as he is the one who guided me from physics to mathematics.

I would like to thank my family and friends for all support. A special expression of gratitude goes to my friend Jeremy Shaw, who helped me with various aspects, especially in C++ programming and Latex coding.

I would like to thank my Ph.D. committee members Dr. Dacian Daescu, Dr. Andres La Rosa and Dr. James Morris for all the work and help they have given me to make this all possible.

Above all of these, I must thank my advisor, Dr. Bin Jiang. His help cannot be expressed adequately in words. There is so much he has help me from getting through various stages of the Ph.D. program, showing me how to teach in a university setting, as well as guiding me to perform academic research and so much more. Dr. Bin Jiang has been truly the best advisor and advocate.

Table of Contents

List of Tables

List of Figures

List of Algorithms

Chapter 1

Finite-Difference Time-Domain Basics

In this chapter, we will go over the basic aspects of the finite-difference time-domain (FDTD) algorithm, one of the most popular numerical methods in computational electrodynamics. Just like most methods in computational electrodynamics, FDTD is built from Maxwell's equations directly, as proposed by Yee in 1966 in his land mark paper [23]. Since then, many improvements have been made towards the FDTD algorithm, such as introduction of Perfectly Match Layers (PML), which introduces an absorbing boundary condition allowing the waves to leave the simulated area without unexpected reflection [2]. The FDTD method surely has its own limitations. The algorithm naturally requires a completely structured grid also known as the Yee grid. However, Many real world problems have complicated geometries which causes troubles when the objects being modeled do not fit the grid very well. This will be discussed in great detail in the next chapter.

On the other hand, FDTD algorithm has many useful characteristics that make it one of the most popular numerical methods in computational electrodynamics. FDTD algorithm is a time marching forward method which easily makes a visual representation of the fields and gives the user a more intuitive insight into the model. This method also scales very well since the number of computation required is proportional to the size of the model and the method requires no large-scale linear algebra computation. The method has been demonstrated to scale linearly, which turns out

to be a good advantage compared with other methods. Another benefit of FDTD is that a single simulation can provide the results for either ultra-waveband temporal waveforms or the sinusoidal steady-state response at any frequency within the excitation spectrum [20].

1.1 Maxwell's Equations and Constitutive Relations

We will show how FDTD algorithm works by building the updating equations from the time-dependent Maxwell's equations. We follow the paper [20] to present both differential and integral forms of the equations. These equations assume there is no electric or magnetic current sources.

Faraday's Law:

$$\frac{\partial \mathbf{B}}{\partial t} = -\nabla \times \mathbf{E} - \mathbf{M} \tag{1.1}$$

$$\frac{\partial}{\partial t} \iint_A \mathbf{B} \cdot d\mathbf{A} = -\oint_l \mathbf{E} \cdot d\mathbf{l} - \iint_A \mathbf{M} \cdot d\mathbf{A} \tag{1.2}$$

Ampere's Law:

$$\frac{\partial \mathbf{D}}{\partial t} = \nabla \times \mathbf{H} - \mathbf{J} \tag{1.3}$$

$$\frac{\partial}{\partial t} \iint_A \mathbf{D} \cdot d\mathbf{A} = \oint_l \mathbf{H} \cdot d\mathbf{l} - \iint_A \mathbf{J} \cdot d\mathbf{A} \tag{1.4}$$

Gauss' Law For the electric field:

$$\nabla \cdot \mathbf{D} = 0 \tag{1.5}$$

$$\oiint_A \mathbf{D} \cdot d\mathbf{A} = 0 \tag{1.6}$$

Gauss' Law For the magnetic field:

$$\nabla \cdot \mathbf{B} = 0 \tag{1.7}$$

$$\oiint_A \mathbf{B} \cdot d\mathbf{A} = 0 \tag{1.8}$$

The Constitutive Relation:

$$\mathbf{D} = \epsilon \mathbf{E} \tag{1.9}$$

$$\mathbf{B} = \mu \mathbf{H} \tag{1.10}$$

where the symbols and their units are defined as below:

$\mathbf{E}$: electric field (volts/meter)

$\mathbf{D}$: electric flux density (coulombs/meter^2)

$\mathbf{H}$: magnetic field (amperes/meter)

$\mathbf{B}$: electric flux density (webers/meter^2)

$\mathbf{J}$: electric current density (amperes/meter^2)

$\mathbf{M}$: equivalent magnetic current density (volts/meter^2)

ϵ : electric permittivity (farads/meter)

μ : magnetic permeability (henrys/meter)

In this paper, both $\mathbf{J}$ and $\mathbf{M}$ are set to zero to simplify the Maxwell's equations. In fact, the constitutive relations can become more complex when the materials become nonlinear and anisotropic. For anisotropic dielectrics, the electric permittivity ϵ, turns out to be a dielectric tensor.

1.2 The Basic Algorithm and Yee Grid

Based on the work of Kane Yee [23], we derive the basic FDTD algorithm to solve the Maxwell's equations. By following Yee's paper, there have been tremendous efforts towards improvements of the basic FDTD algorithm. The current form of the basic algorithm is outlined in Algorithm 1.1.

To build the updating equations for the electric and magnetic fields, we first apply

Algorithm 1.1: Outline of FDTD

1: Build a space incorporating the tested device with PMLs
2: Set all fields equal to zero
3: **repeat**
4: Update **D** from **H**
5: Update **E** from **D**
6: Preform needed changes to handle **E** -field source
7: Update **B** from **E**
8: Update **H** from **B**
9: Preform needed changes to handle **H** -field source
10: Record field data
11: **until** enough cycles have been run then show the results
12: Perform post-processes on the recorded data

finite difference scheme to the Maxwell's equations.

$$\begin{aligned} \nabla \times \mathbf{E}(t) &= -\frac{\partial \mathbf{B}(t)}{\partial t} \\ &= -\frac{\mathbf{B}|_{(t+\frac{\Delta t}{2})} - \mathbf{B}|_{(t-\frac{\Delta t}{2})}}{\Delta t} \end{aligned} \tag{1.11}$$

and

$$\begin{aligned} \nabla \times \mathbf{H}(t+\tfrac{\Delta t}{2}) &= \frac{\partial \mathbf{D}(t)}{\partial t} \\ &= \frac{\mathbf{D}|_{(t+\Delta t)} - \mathbf{D}|_{(t)}}{\Delta t} \end{aligned} \tag{1.12}$$

Then the updating equations can be formed using (1.11) and (1.12) as below:

$$\mathbf{B}|_{(t+\frac{\Delta t}{2})} = \mathbf{B}|_{(t-\frac{\Delta t}{2})} - \Delta t(\nabla \times \mathbf{E}|_{(t)}) \tag{1.13}$$

and

$$\mathbf{D}|_{(t+\Delta t)} = \mathbf{D}|_{(t)} + \Delta t(\nabla \times \mathbf{H}|_{(t)}) \tag{1.14}$$

It is important to note that these updating equations stagger **E** and **H** fields in time, where **E** is updated at the whole time steps while **H** is updated at the half time steps. Therefore we only know **E** or **H** at a given time, and have to interpolate one or the other to have them at the same time. This can be done by using midpoint rule in our finite difference scheme.

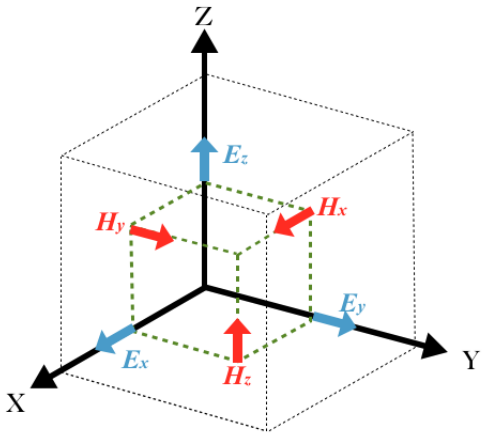

Figure 1.1: A classic unit cell in the Yee grid as the black dotted line box where the E-components are at the midpoints of the edges and H-components are at the centers of the faces. This figure is a reproduction from [19].

In Figure 1.1, you can see that not only **E** and **H** stagger in time, but each component of the fields **E** and **H** also stagger in space. This elegant design solve the Maxwell's equations efficiently. By setting up the field components in this way, the algorithm is naturally divergence free, thereby satisfying Gauss' laws directly.

Under the situation of diagonal dielectric tensors, the Maxwell's equations along

with constitutive relation (1.13) and (1.14) become

$$
\begin{aligned}
E_x|_{(t+\Delta t)} &= E_x|_{(t)} + \frac{\Delta t}{\epsilon_{xx}}\left(\frac{\partial H_z}{\partial y} - \frac{\partial H_y}{\partial z}\right) \\
E_y|_{(t+\Delta t)} &= E_y|_{(t)} + \frac{\Delta t}{\epsilon_{yy}}\left(\frac{\partial H_x}{\partial z} - \frac{\partial H_z}{\partial x}\right) \\
E_z|_{(t+\Delta t)} &= E_z|_{(t)} + \frac{\Delta t}{\epsilon_{zz}}\left(\frac{\partial H_y}{\partial x} - \frac{\partial H_x}{\partial y}\right) \\
H_x|_{(t+\frac{\Delta t}{2})} &= H_x|_{(t-\frac{\Delta t}{2})} - \frac{\Delta t}{\mu_{xx}}\left(\frac{\partial E_z}{\partial y} - \frac{\partial E_y}{\partial z}\right) \\
H_y|_{(t+\frac{\Delta t}{2})} &= H_y|_{(t-\frac{\Delta t}{2})} - \frac{\Delta t}{\mu_{yy}}\left(\frac{\partial E_x}{\partial z} - \frac{\partial E_z}{\partial x}\right) \\
H_z|_{(t+\frac{\Delta t}{2})} &= H_z|_{(t-\frac{\Delta t}{2})} - \frac{\Delta t}{\mu_{zz}}\left(\frac{\partial E_y}{\partial x} - \frac{\partial E_x}{\partial y}\right)
\end{aligned}
\tag{1.15}
$$

Then by applying finite different scheme, we get the electric and magnetic field up-

dating equations as below.

$$
\begin{aligned}
E_x|_{(t+\Delta t)} &= E_x|_{(t)} + \frac{\Delta t}{\epsilon_{xx}} \left(\frac{H_z^{i,j,k}|_{(t+\frac{\Delta t}{2})} - H_z^{i,j-1,k}|_{(t+\frac{\Delta t}{2})}}{\Delta y} \right. \\
&\qquad \left. - \frac{H_y^{i,j,k}|_{(t+\frac{\Delta t}{2})} - H_y^{i,j,k-1}|_{(t+\frac{\Delta t}{2})}}{\Delta z} \right) \\
E_y|_{(t+\Delta t)} &= E_y|_{(t)} + \frac{\Delta t}{\epsilon_{yy}} \left(\frac{H_x^{i,j,k}|_{(t+\frac{\Delta t}{2})} - H_x^{i-1,j,k}|_{(t+\frac{\Delta t}{2})}}{\Delta z} \right. \\
&\qquad \left. - \frac{H_z^{i,j,k}|_{(t+\frac{\Delta t}{2})} - H_z^{i-1,j,k}|_{(t+\frac{\Delta t}{2})}}{\Delta x} \right) \\
E_z|_{(t+\Delta t)} &= E_z|_{(t)} + \frac{\Delta t}{\epsilon_{zz}} \left(\frac{H_y^{i,j,k}|_{(t+\frac{\Delta t}{2})} - H_y^{i-1,j,k}|_{(t+\frac{\Delta t}{2})}}{\Delta x} \right. \\
&\qquad \left. - \frac{H_x^{i,j,k}|_{(t+\frac{\Delta t}{2})} - H_x^{i,j-1,k}|_{(t+\frac{\Delta t}{2})}}{\Delta y} \right) \\
H_x|_{(t+\frac{\Delta t}{2})} &= H_x|_{(t-\frac{\Delta t}{2})} - \frac{\Delta t}{\mu_{xx}} \left(\frac{E_z^{i,j+1,k}|_t - E_z^{i,j,k}|_t}{\Delta y} - \frac{E_y^{i,j,k+1}|_t - E_y^{i,j,k}|_t}{\Delta z} \right) \\
H_y|_{(t+\frac{\Delta t}{2})} &= H_y|_{(t-\frac{\Delta t}{2})} - \frac{\Delta t}{\mu_{yy}} \left(\frac{E_x^{i,j,k+1}|_t - E_x^{i,j,k}|_t}{\Delta z} - \frac{E_z^{i+1,j,k}|_t - E_z^{i,j,k}|_t}{\Delta x} \right) \\
H_z|_{(t+\frac{\Delta t}{2})} &= H_z|_{(t-\frac{\Delta t}{2})} - \frac{\Delta t}{\mu_{zz}} \left(\frac{E_y^{i+1,j,k}|_t - E_y^{i,j,k}|_t}{\Delta x} - \frac{E_x^{i,j+1,k}|_t - E_x^{i,j,k}|_t}{\Delta y} \right)
\end{aligned} \tag{1.16}
$$

As you can see in Figure 1.2, the H_z component is located at the midpoint of two neighboring E_y components and also at the midpoint of neighboring two E_x components. This also hold for all other five field components. In Section 3.1, we will develop new updating equations for H_z, E_x and E_y components cross the interface of two different dielectric media based on the integral form of the Maxwell's equations.

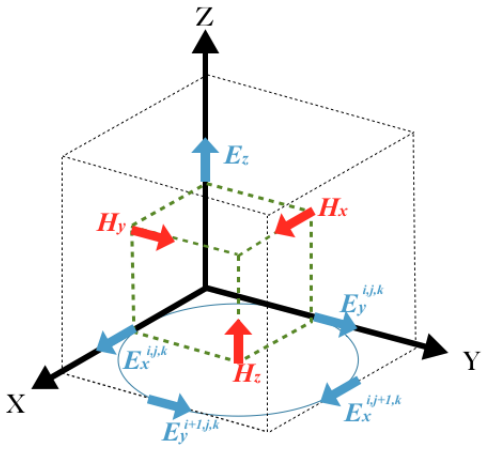

Figure 1.2: A classic unit cell in the Yee grid with a representation of the updating equation for H_z, located at the midpoint of two E_y terms and the midpoint of two E_x terms. This figure is a reproduction from [19].

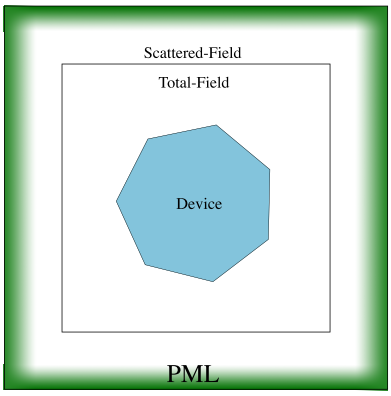

Figure 1.3: A common setup for a two dimensional FDTD. The total-field and scattered-field under white background are separated by solid lines and PML layer is shown as green along the edge.

1.3 Aspects of Running the FDTD Algorithm

In Figure 1.3, we implement a two dimensional FDTD algorithm. The total field is the inner region which is simulated by the FDTD and the scattered field is the outer region which only count for the scattered field thus allowing the waves to leave the

simulated area. In order to excite the fields, an incident wave source is excited within the total-field region. The source is not counted in the scattering-field. Meanwhile, a perfectly matched layer(PML) absorbing boundary condition is also introduced around the scatter field region. The PML layer ensures the system absorbs incoming electromagnetic waves to let the waves leave the whole region without any unexpected reflection.

The FDTD implementation in two dimensional environment can be easily extended to one or three dimensional scenarios. Since the topics of total-field/scattered-field, PML boundary condition, and incident wave source are not the focus of this dissertation, we do not discuss them in more details.

Chapter 2

Literature Review

In this chapter, we will review the most recent improvements on the FDTD algorithm as a foundation of our new scheme presented in the next chapter. In particular, we will focus on the related literature that use FDTD method to solve the Maxwell's equations within a domain consisting of multiple media with distinct permittivities. This leads to discontinuity for discretization of the Maxwell's equations across the interface between different media.

The original FDTD algorithm proposed in Yee's paper assigned each of the field component an electric permittivity and a magnetic permeability solely based on the material properties at its location [23]. The discretization of the field components can lead to the meshed shape of the device quite different from its real shape as shown in Figure 2.1. This is commonly known as the staircasing or pixelation problem. Therefore, the original algorithm proposed by Yee has been regarded as the staircasing method.

This pixelation introduces an error in the FDTD algorithm. In general, the staircasing has an error that scales with $\mathcal{O}(\Delta x^2)$ given a grid size of Δx for cells that are homogenous. However, in cells that contain a media interface, the local error becomes $\mathcal{O}(1)$. Even though the number of cells that contain an interface is often a small fraction of the total cells, these local errors can cause a rough global error of $\mathcal{O}(\Delta x)$. Furthermore, small changes in the grid in either size or position could induce

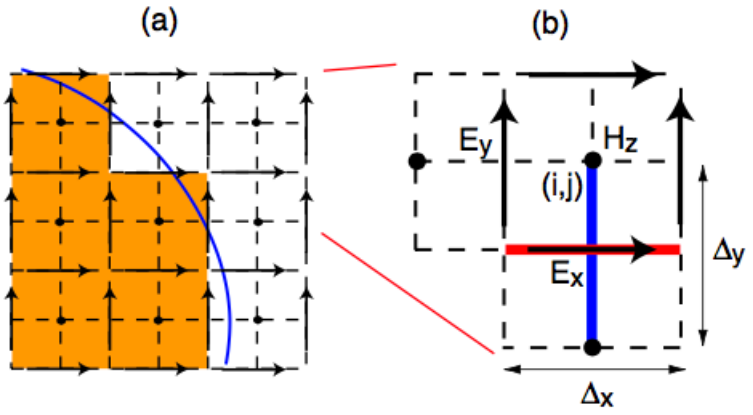

Figure 2.1: (a)The staircasing method to model devices with curved surfaces leads to heavy pixelation; (b) A close look up of the field components. This figure is a reproduction from [17].

large changes for the global error. Therefore, it is possible that decreases in grid size could lead to a substantial increase in the global error of the algorithm. Such sporadic behavior of the error makes the staircasing method undesirable for many cases [21].

2.1 Approaches to Overcome the Pixelation Problem

Recent research in modern optics and electromagnetism dealing with the Maxwell's equations have focused on more and more complex geometries with different materials so that the complicated dielectric tensor can cause serious pixelation issues. In turn, there have been many improvements in FDTD algorithms to overcome these pixelation issues. The main goal of these research resutls is to ensure the FDTD algorithm still retains the second-order global error in a non-homogenous domain consisting of multiple media. However, many proposed algorithms not only increase the algorithm complexity significantly, but also lose the benefits of the FDTD algorithm. In order to maintain the benefits of the FDTD algorithm, the following approaches have been proposed. Each of them has its own merits and drawbacks.

One way to overcome the pixelation problem is by fitting the mesh to the device, thereby generating the so-called non-orthogonal FDTD. As seen in Figure 2.2, the constructed mesh provides an accurate representation of the device [7]. Even though this method converges faster than the standard FDTD method, it suffers from many problems. The complexity of the algorithm is much larger than original FDTD method as this method is a hybrid of FDTD and finite element method (FEM). Meanwhile, it has well-known time stability issues [4].

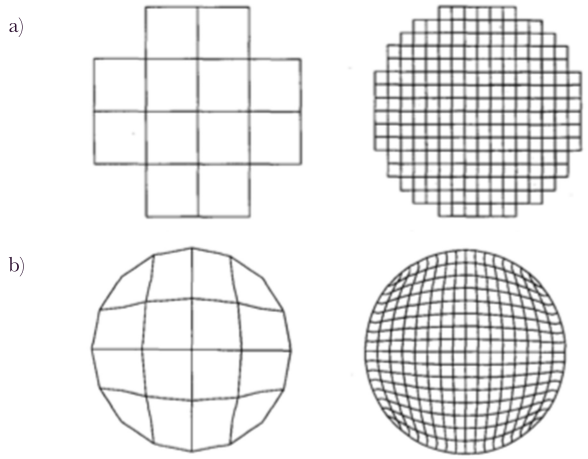

Figure 2.2: Showing the comparison of orthogonal mesh (a) and nonorthogonal mesh (b) of a cylinder in a 2D setup [7]. This figure is a reproduction from [7].

Another method is to keep the orthogonal grid but refine the mesh around the cells close to the interfaces, also known as the sub-griding method. Much like the Finite element method, this method just decreases the mesh size in those neighboring cells in order to increase the accuracy of the algorithm while keeping the computation load increase as minimal as possible [14]. The problem of this method occurs at the boundary of the two different meshes as seen in figure Figure 2.3. Not only the locations of field components may not match at the boundary, but the calculation of the field components at the boundary is also complicated since the adjacent field

components may not exist. The main concern of this method is how to handle the boundary of two different meshes to ensure the method is both stable and accurate.

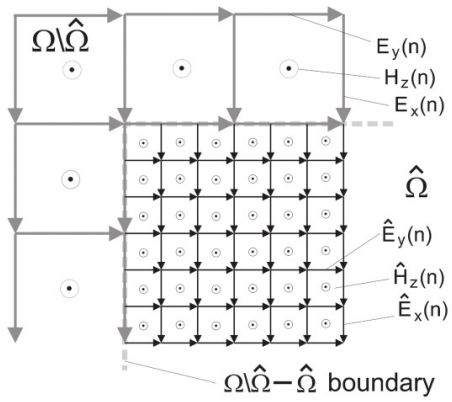

Figure 2.3: The boundary of the original grid and the subgrid with refinement factor r = 3 on a 2D orthogonal TE case, showing how some of the boundary field components require modified updating equation. This figure is a reproduction from [14].

To keep a completely structured grid and maintain all the benefits of FDTD, another method redefines Maxwell's integral equations around the boundary of the device to match its contour. This is known as the contour-path (CP) FDTD, as seen in Figure 2.4. This method has specialized updating equations for each cell near the boundary, and some field components go unused, some are borrowed from the nearest neighbor and some field components must be interpolated [12]. The benefits of this method is that it only slightly increase the CPU time and memory load. However, the requirement of borrowing the nearest neighbor can give rise to instabilities issues [4]. Also there is some loss of the accuracy since some field components are unused by the algorithm.

The methods discussed in the next section will be the focus of this dissertation. They use so-called sub-pixel smoothing techniques to change the permittivities of the field components in order to produce better results by taking account of many different factors, such as the interface conditions, permittivities of adjacent field components

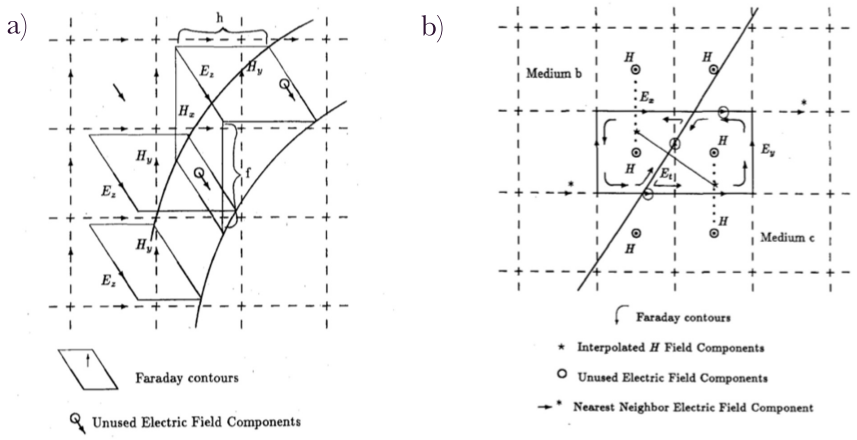

Figure 2.4: (a) shows the Faraday contours. (b) shows the changes in the Faraday updating equations to match the boundary condition of the device. This figure is a reproduction from [12].

and so on. While there are various approaches as shown in the next section, these effective permittivities smooth out the pixel error or at the very least stabilize it. The main benefit of these methods is that there is a negligible increase of the numerical load since all the permittivities have been calculated beforehand and stored in a matrix before the main FDTD algorithm loop. Also, these effective permittivities can handle many situations and can be combined with other methods seamlessly.

2.2 Methods of Sub-pixel Smoothing and Effective Permittivities

The key point in developing a method for sub-pixel smoothing is to compute effective permittivities for all the cells around the boundary, even for devices with very simple geometries, as in seen in Figure 2.5. The earliest method of sub-pixel smoothing is the volume average effective permittivity (V-EP) because of its simple implementation. This method assigns effective permittivities for all the field components in a cell that contains media boundary. The effective permittivities are calculated by taking a weighted average based on how much percent of the volume each medium occupies.

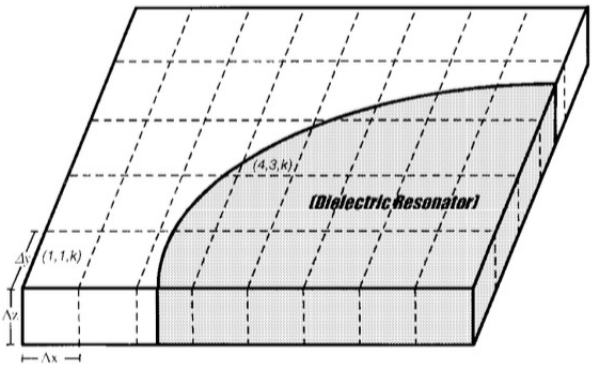

Figure 2.5: One-quarter cross-section of a dielectric cylinder showing a surface cause many ways to determine effective permittivity. This figure is a reproduction from [5].

The equation is as follows.

$$\epsilon_{eff} = V_{\epsilon_1}(i,j,k) * \epsilon_1 + (1 - V_{\epsilon_1}(i,j,k)) * \epsilon_2 \tag{2.1}$$

Where $V_{\epsilon_1}(i,j,k)$ is the ratio of the volume of the (i,j,k) cell occupied by the material with permittivity ϵ_1 over the whole cell volume [5].

This method is very simple for implementation, quite intuitive and has very low computation cost. Moreover, it greatly stabilizes the error fluctuation that occurs in the staircasing method. All these factors have made this method quite popular [5]. The big drawback of this method is that it does not decrease the error rapidly and in some situations, its error can be worse than staircasing method.

It was quickly noticed that boundary conditions played an important role in determining effective permittivity in order to maintain the algorithm's accuracy. In particular, those methods based on perturbation theory to fix the pixelation problem failed to predict the lowest-order behavior and often gave incorrect results if the electric permittivity was discontinuous at the interface of the media. Such problems were compounded when the permittivity of the device became a dielectric tensor.

Therefore, new smoothing methods which forces the continuous electric dielectric permittivity were proposed to overcome these issues [11].

The first attempts of smoothing the dielectric permittivity resolved some of the problems with discontinuous permittivities but caused new issues. Some of the new smoothing methods ended up with worse errors than FDTD algorithms without any smoothing. The main problem was identified as not always satisfying the interface conditions for electromagnetic fields, that is, the component of $\mathbf{E}$ parallel to the interface ($\mathbf{E}_{\parallel}$) and the component of $\mathbf{D}$ perpendicular to the interface ($\mathbf{D}_{\perp}$) should be continuous across the material interface. To address this issue, an effective dielectric tensor was proposed for isotropic materials as follows.

$$\epsilon^{-1} = \mathbf{P}[\epsilon^{-1}] + (1 - \mathbf{P})[\epsilon]^{-1} \tag{2.2}$$

where $\mathbf{P}$ is the projection matrix $P_{ij} = n_i n_j$ onto the normal direction of the interface, $[\epsilon^{-1}]$ and $[\epsilon]$ are the volume average of ϵ^{-1} and ϵ in each cell [6].

This proposed method which satisfies interface conditions for electromagnetic fields in equation 2.2 was shown later to have late-time instabilities. To overcome this, many possibilities to average the effective dielectric tensor were explored as seen in Figure 2.6. Part (c) of Figure 2.6 was the one that was chosen since it made the effective dielectric tensor symmetric and positive semi-definite. The new method replacing (b) by (c) as seen in Figure 2.6 ensured all the eigenvalues are non-negative so that eigenmodes have real frequencies in the standard Yee algorithm to avoid late time instabilities caused by complex frequencies [22]. After that, subsequent work on the effective dielectric tensor continued and began to include general anisotropic materials, until they could achieve convergence between first-order and second-order [13], [18]. The most recent scheme that has shown the highest accuracy takes the

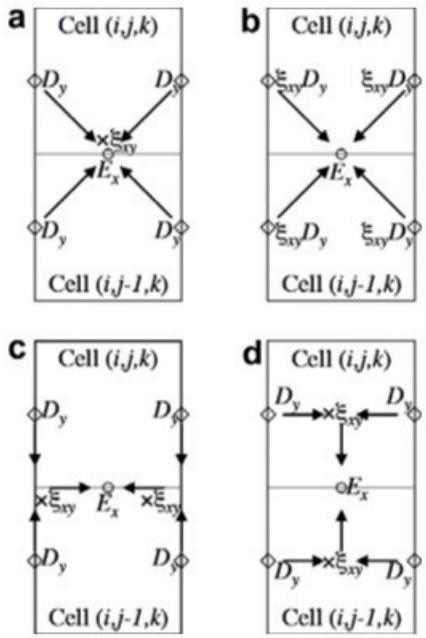

Figure 2.6: Four methods of interpolating E_x by using ϵ_{xy} and its neighboring values of D_y. (b) was used [6] until (c) was proven to be the only stable scheme in [22]. This figure is a reproduction from [22].

average of eight "triplets" as shown in Figure 2.7 [1].

Although the method shown in Figure 2.7 is highly accurate, this effective dielectric tensor denoted as ϵ_{acc} can still be asymmetric thus unstable for certain conditions. Therefore the last improvement of the effective dielectric tensor makes it symmetric as seen below [21].

$$\epsilon_{eff} = \frac{1}{2}(\epsilon_{acc} + \epsilon_{acc}^{\mathrm{T}}) \tag{2.3}$$

While the method reduces the accuracy of those cells containing the interface to a local error of $\mathcal{O}(1)$, the local error for the homogenous cells is still $\mathcal{O}(\Delta x^2)$. This gives a global error as $\mathcal{O}(\Delta x)$. The numerical results showed that this scheme gives the best result in general and the error in practice lies in between first and second-order

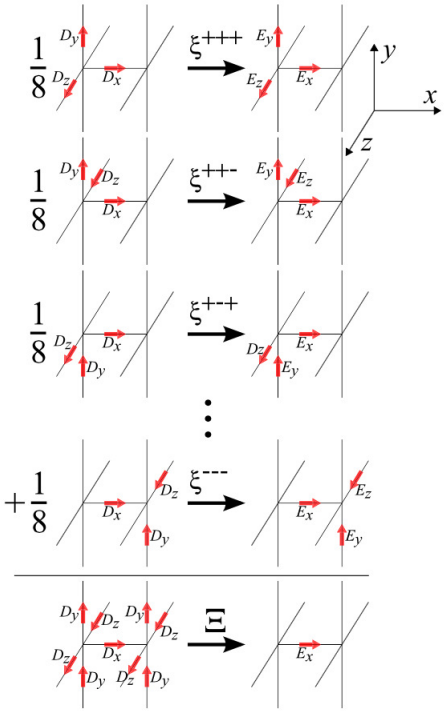

Figure 2.7: This figure demonstrates how the effective dielectric tensor is calculated by averaging eight "triplets" in the most recent schemes achieving the highest accuracy. This figure is a reproduction from [21].

in most cases.

Therefore, the effective permittivities (dielectric tensor) has to be constructed carefully to avoid instabilities by paying close attention to the properties of both the tensor and the fields components along the boundary. In the next section, we will introduce a new 2D FDTD algorithm to solve the Maxwell's equations in multiple media with constant permittivities and demonstrate that this algorithm can achieve second-order convergence when the material interface is orthogonal to the Yee grid.

2.3 A Second-Order FDTD Algorithm for Transverse Electric Case

As reported in the literature, no subpixel smoothing method that works in the full 3D FDTD algorithm can achieve second-order convergence. However, if the FDTD

algorithm is applied to a 2D transverse electric(TE) case, it may achieve the second-order convergence. For the TE case, the six electric and magnetic field components are reduced to three components. That is, there are two electric field components and one magnetic component, as shown in Figure 2.8. The other case is the transverse magnetic (TM) case where the the one-component electric field is always continuous across the boundary so there is no need to construct effective permittivities as in TE case. Therefore, our research always focuses on the challenging TE case and ignores the trivial TM case.

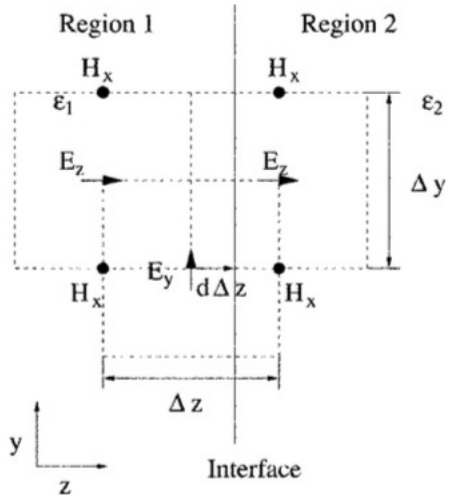

Figure 2.8: The TE FDTD configuration with material interface orthogonal to the Yee grid. This figure is a reproduction from [10].

One of the second-order methods can achieve second order convergence only if the media interface is orthogonal to the Yee grid as seen in Figure 2.8. The electric fields are constructed as follows:

$$E_{y_{(j,k)}}^{n+1} = E_{y_{(j,k)}}^{n} + \frac{\Delta t}{\epsilon_y^* \Delta z}\left(H_{x_{(j,k+\frac{1}{2})}}^{n+\frac{1}{2}} - H_{x_{(j,k-\frac{1}{2})}}^{n+\frac{1}{2}}\right) + \mathcal{O}(\Delta t^2) + \mathcal{O}(\Delta z^2) \tag{2.4}$$

where

$$\epsilon_y^* = \left(\frac{1}{2} + d\right)\epsilon_1 + \left(\frac{1}{2} - d\right)\epsilon_2 \tag{2.5}$$

where d is the distance to the interface from the edge of the unit cell as seen in Figure 2.8, and

$$E_{z_{(j,k)}}^{n+1} = E_{z_{(j,k)}}^{n} + \frac{\Delta t}{\epsilon_z^* \Delta z}\left(H_{x_{(j+\frac{1}{2},k)}}^{n+\frac{1}{2}} - H_{x_{(j-\frac{1}{2},k)}}^{n+\frac{1}{2}}\right) + \mathcal{O}(\Delta t^2) + \mathcal{O}(\Delta y^2) \tag{2.6}$$

where

$$\frac{1}{\epsilon_z^*} = \frac{d}{\epsilon_1} + \frac{1-d}{\epsilon_2} \tag{2.7}$$

It will be shown in the next chapter that our new algorithm can be reduced to the same equations when the boundary interface in those cells is orthogonal to the Yee grid.

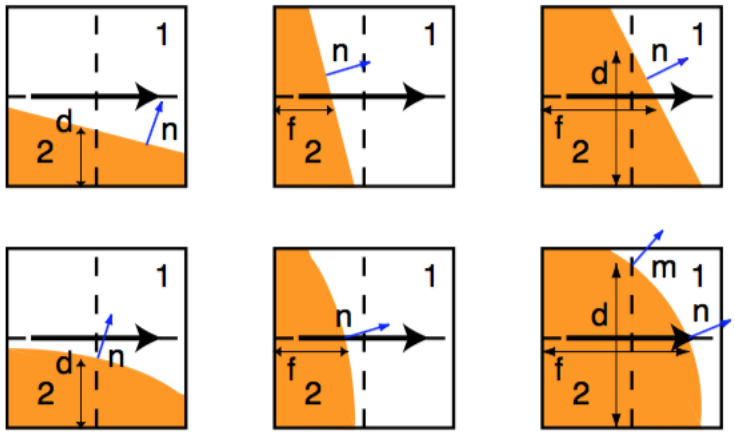

Figure 2.9: Various material interface boundaries in a unit cell for CP-EP method. This figure is a reproduction from [17].

This work was then extended to the so-called contour-path effective permittivities

(CP-EP) method [17]. This CP-EP method first addressed the orthogonal cases as shown above, then extended to handle with more general geometry. Unlike the previous method, it could handle arbitrary boundary with any orientation of the boundary which is sufficiently smooth as seen in Figure 2.9. Since there are various kinds of effective permittivities constructed in their work, we will only show one example of CP-EP schemes as follows.

$$\int_{(j-1)\Delta y}^{j\Delta y} D_x dy = \{d[\epsilon_1 n^2 + \epsilon_2(1-n^2)] + (\Delta y - d)\epsilon_1\} E_x \tag{2.8}$$

Compared with traditional staircasing methods, the CE-EP method has almost no additional runtime cost since determination of the effective permittivities has been done before the main FDTD loop.

However, we will demonstrate in the next chapter that this method is incomplete and does not incorporate one important term from the interface conditions into the numerical FDTD algorithm. We will then develop a new FDTD algorithm for the 2D TE case where the missing term will be re-considered in order to produce a more accurate and stable algorithm.

There are two more research work that also need to be mentioned in this literature review chapter. The first one included the electromagnetic field boundary condition in a complete sense and has shown second order convergence [16]. However, this algorithm added many terms and has an additional step in the main FDTD loop to increase numerical load significantly. The second work used the reflection coefficients to derived effective permittivities and showed the algorithm can also achieve a second-order convergence with several slanted angles between the interface and the Yee grid rather than just orthogonal to the Yee grid [8], [9]. However, its derivation was quite complicated and had no ways to be extended to arbitrary interface. Due

to their extreme computational complexity, we will leave both of them outside our consideration range.

In subsequent chapters, we will introduce our new method that is shown to have second order convergence theoretically. We will add a few terms to the boundary cells when necessary so as to keep the numerical load increase as minimum as possible. Then our numerical tests can clearly verify that our algorithm has a much better performance than CP-EP algorithm, VEP algorithm and staircasing algorithm while still maintaining numerical stability. Our research work has been published in Journal ***Nanotechnology*** [15] and another paper is currently under preparation for future submission to Journal ***Optics Express***.

Chapter 3

New Second Order FDTD Schemes

In this chapter, we will propose a new second order finite difference time domain method to solve Maxwell's equations in a domain composed of two different media with different electric permittivities. To simply the algorithm description, we will focus on the most important transverse electric (TE) scenario. That is, $\mathbf{E}(x, y) = E_x\mathbf{i} + E_y\mathbf{j}$ is located in the incident xy-plane while $\mathbf{H}(x, y) = H_z\mathbf{k}$ is along z-axis. Moreover, we restrict our discussion to dielectric and non-magnetic media such that $\mathbf{D}(x, y) = \epsilon\mathbf{E}(x, y)$ and $\mathbf{B}(x, y) = \mathbf{H}(x, y)$ where ϵ stays as a constant in different media. Based on the integral version of the Maxwell equations, we derive the new second-order algorithm for any orientation of the interface. This is a significant improvement over all current methods which can only achieve second-order convergence under specific angles between the interface and Cartesian coordinate system, such as parallel or orthogonal to x-axis.

3.1 Second-order FDTD Scheme in Homogeneous Medium

In this section, we will derive FDTD scheme bases on the integral forms of Maxwell's equations and show that the scheme has indeed achieved second-order convergence in a uniform homogeneous medium. As usual, the incident xy-plane is discretized by using space increments Δx and Δy along x and y axis, respectively.

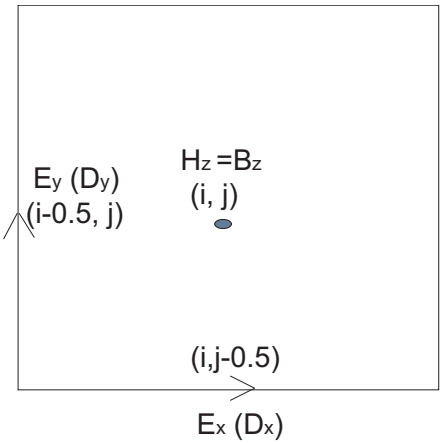

Figure 3.1: Positions of $\mathbf{D}(\mathbf{E})$ and $\mathbf{H}(\mathbf{B})$

According to the Yee scheme, $H_z(B_z), E_x(D_x)$ and $E_y(D_y)$ are positioned at locations (i, j), $(i, j - \frac{1}{2})$ and $(i - \frac{1}{2}, j)$ respectively, as shown in Figure 3.1.

Let us express Faraday's law integral form

$$\frac{\partial}{\partial t} \iint_S \mathbf{B} \cdot \mathbf{n} dS = - \oint_{\partial S} \mathbf{E} \cdot d\mathbf{l} \tag{3.1}$$

and Ampere's law in integral form

$$\frac{\partial}{\partial t} \iint_S \mathbf{D} \cdot \mathbf{n} dS = \oint_{\partial S} \mathbf{H} \cdot d\mathbf{l} \tag{3.2}$$

First, let's discretize Faraday's law (3.1) as follows: Choose S to be the rectangular box centered at (i, j). then the unit norm vector of S is $\mathbf{n} = \mathbf{k}$ along z axis and ∂S denoted the four sides of the rectangle shown in Figure 3.2.

Discretization of the left hand side term of (3.1) at time t_n by centered finite difference scheme yields:

$$\frac{\iint_S \mathbf{H}^{n+\frac{1}{2}} \cdot \mathbf{n} dS - \iint_S \mathbf{H}^{n-\frac{1}{2}} \cdot \mathbf{n} dS}{\Delta t} = - \oint_{\partial S} \mathbf{E}^n \cdot d\mathbf{l} + \mathcal{O}(\Delta t \Delta x \Delta y) \tag{3.3}$$

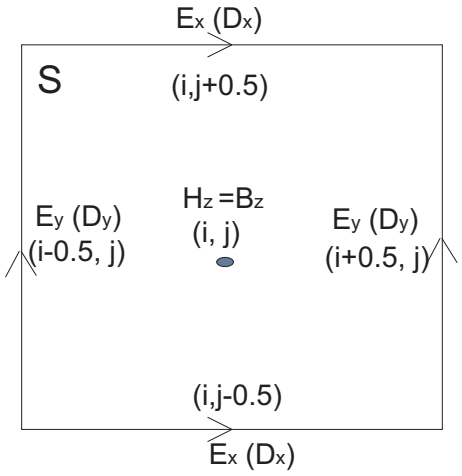

Figure 3.2: Discretization of Faraday's law

or

$$\iint_S \mathbf{H}^{n+\frac{1}{2}} \cdot \mathbf{n} dS = \iint_S \mathbf{H}^{n-\frac{1}{2}} \cdot \mathbf{n} dS - \Delta t \oint_{\partial S} \mathbf{E}^n \cdot d\mathbf{l} + \mathcal{O}(\Delta t^2 \Delta x \Delta y) \tag{3.4}$$

which can be simplified as

$$\begin{aligned} \int_{(i-\frac{1}{2})\Delta x}^{(i+\frac{1}{2})\Delta x} \int_{(j-\frac{1}{2})\Delta y}^{(j+\frac{1}{2})\Delta y} H_z^{n+\frac{1}{2}} dxdy &= \int_{(i-\frac{1}{2})\Delta x}^{(i+\frac{1}{2})\Delta x} \int_{(j-\frac{1}{2})\Delta y}^{(j+\frac{1}{2})\Delta y} H_z^{n-\frac{1}{2}} dxdy \\ &- \Delta t \left[\int_{(i-\frac{1}{2})\Delta x}^{(i+\frac{1}{2})\Delta x} E^n_{(x,j-\frac{1}{2})} dx + \int_{(j-\frac{1}{2})\Delta y}^{(j+\frac{1}{2})\Delta y} E^n_{(i+\frac{1}{2},y)} dy - \int_{(i-\frac{1}{2})\Delta x}^{(i+\frac{1}{2})\Delta x} E^n_{(x,j+\frac{1}{2})} dx \right. \\ &\left. - \int_{(j-\frac{1}{2})\Delta y}^{(j+\frac{1}{2})\Delta y} E^n_{(i-\frac{1}{2},y)} dy \right] + \mathcal{O}(\Delta t^2 \Delta x \Delta y) \end{aligned} \tag{3.5}$$

where the terms in [ ] denotes $\oint_{\partial S} \mathbf{E}^n \cdot d\mathbf{l}$.

Applying integration midpoint rule to all the integrals in the last equation yields

$$\begin{aligned} H^{n+\frac{1}{2}}_{z_{(i,j)}} \Delta x \Delta y &= H^{n-\frac{1}{2}}_{z_{(i,j)}} \Delta x \Delta y - \Delta t [E^n_{x_{(i,j-\frac{1}{2})}} \Delta x + E^n_{y_{(i+\frac{1}{2},j)}} \Delta y - E^n_{x_{(i,j+\frac{1}{2})}} \Delta x \\ &- E^n_{y_{(i-\frac{1}{2},j)}} \Delta y] + \mathcal{O}(\Delta x^3 \Delta y) + \mathcal{O}(\Delta x^3 \Delta t) + \mathcal{O}(\Delta y^3 \Delta t) + \mathcal{O}(\Delta t^2 \Delta x \Delta y) \end{aligned} \tag{3.6}$$

Divining both sides by $\Delta x \Delta y$ and noticing $\Delta x \sim \Delta y \sim \Delta t$ with $\Delta x \Delta t \leq \frac{1}{2}\Delta x^2 + \frac{1}{2}\Delta t^2$, we obtain

$$H_{z_{(i,j)}}^{n+\frac{1}{2}} = H_{z_{(i,j)}}^{n-\frac{1}{2}} - \Delta t[\frac{E_{x_{(i,j-\frac{1}{2})}}^{n} - E_{x_{(i,j+\frac{1}{2})}}^{n}}{\Delta y} + \frac{E_{y_{(i+\frac{1}{2},j)}}^{n} - E_{y_{(i-\frac{1}{2},j)}}^{n}}{\Delta x}] + \mathcal{O}(\Delta x^2) + \mathcal{O}(\Delta y^2) + \mathcal{O}(\Delta t^2) \tag{3.7}$$

which shows that discretization of Faraday's law by Yee Scheme generates second-order algorithm to update $H_z^{n+\frac{1}{2}}$ term within a uniform medium.

Secondly we will discretize Ampere's law (3.2) to update E_x^n and E_y^n respectively as follows:

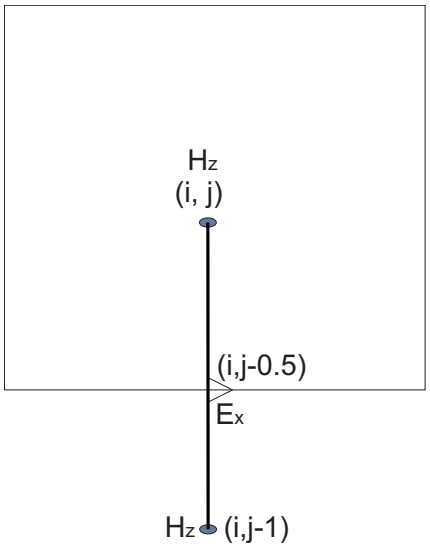

Figure 3.3: Discretization of Ampere's law

To update E_x^n, choose S in (3.2) to be a rectangle in yz-plane whose projection on the xy-plane is the line segment L_0 from node $(i, j-1)$ to node (i, j) and whose height is Δz. Then the unit norm vector of S is $\vec{i}$ along x-axis and ∂S is composed of four line segments: $L_0, L_{\Delta z}$ which is parallel with L_0 with Δz apart, and other two line segments perpendicular to L_0 in yz-plane. Since both $\mathbf{E}$ and $\mathbf{H}$ are independent

of z, (3.2) becomes

$$\frac{d}{dt}\int_{(j-1)\Delta y}^{j\Delta y} \epsilon E_{x_{(i,y)}} dy \cdot \Delta z = H_{z_{(i,j)}} \cdot \Delta z - H_{z_{(i,j-1)}} \cdot \Delta z \tag{3.8}$$

Discretization of the left hand side at time $t_{n+\frac{1}{2}}$ by center finite difference scheme yields

$$\epsilon \frac{\int_{(j-1)\Delta y}^{j\Delta y} E^{n+1}_{x_{(i,y)}} dy - \int_{(j-1)\Delta y}^{j\Delta y} E^{n}_{x_{(i,y)}} dy}{\Delta t} = H^{n+\frac{1}{2}}_{z_{(i,j)}} - H^{n+\frac{1}{2}}_{z_{(i,j-1)}} + \mathcal{O}(\Delta t \Delta y) \tag{3.9}$$

Applying integration midpoint rule to all integrals in (3.9) yields

$$\epsilon \left(E^{n+1}_{x_{(i,j-\frac{1}{2})}} - E^{n}_{x_{(i,j-\frac{1}{2})}} \right) \cdot \Delta y = \Delta t \left(H^{n+\frac{1}{2}}_{z_{(i,j)}} - H^{n+\frac{1}{2}}_{z_{(i,j-1)}} \right) + \mathcal{O}(\Delta y^3) + \mathcal{O}(\Delta t^2 \Delta y) \tag{3.10}$$

which can be simplified as

$$E^{n+1}_{x_{(i,j-\frac{1}{2})}} = E^{n}_{x_{(i,j-\frac{1}{2})}} + \frac{\Delta t}{\epsilon} \frac{H^{n+\frac{1}{2}}_{z_{(i,j)}} - H^{n+\frac{1}{2}}_{z_{(i,j-1)}}}{\Delta y} + \mathcal{O}(\Delta y^2) + \mathcal{O}(\Delta t^2) \tag{3.11}$$

Which also shows that discretization of Ampere's law by Yee scheme generates second-order algorithm to update E^{n+1}_x term within a uniform medium.

Similarly, we can discretize (3.2) to update E^{n+1}_y at $(i-\frac{1}{2}, j)$ by choosing S to be a rectangle in xz-plane with one side from node $(i-1, j)$ to node (i, j) as follows:

$$E^{n+1}_{y_{(i-\frac{1}{2},j)}} = E^{n}_{y_{(i-\frac{1}{2}.j)}} + \frac{\Delta t}{\epsilon} \frac{H^{n+\frac{1}{2}}_{z_{(i-1,j)}} - H^{n+\frac{1}{2}}_{z_{(i,j)}}}{\Delta x} + \mathcal{O}(\Delta x^2) + \mathcal{O}(\Delta t^2) \tag{3.12}$$

3.2 Relation of $\mathbf{D}(x, y)$ and $\mathbf{E}(x, y)$ Across the Interface

In order to set up the new second-order FDTD method to solve Maxwell's equations in a domain composed of two different media, we need to find the relation of $\mathbf{D}(x, y)$ and $\mathbf{E}(x, y)$ across the interface of these two media. It is well known that $\mathbf{H}(x, y)$ is continuous in the whole domain composed of two different media. Meanwhile, across the interface between these two media, the tangential component $\mathbf{E}_\tau(x, y)$ of the electric field and the normal component $\mathbf{D}_n(x, y)$ of the electric flux are continuous as well. In this section, we will utilize this fact to derive the relation of $\mathbf{E}(x, y)$ and $\mathbf{D}(x, y)$ across the interface Γ as show in figure 3.4 where $\mathbf{n} = (n_x, n_y)$ is the outward unit norm vector from region 1.

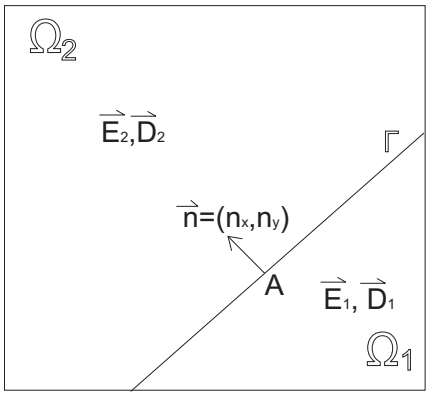

Figure 3.4: Relation of $\mathbf{D}$ and $\mathbf{E}$ across Γ

Choose $A \in \Gamma$. Let's set up the relation between $\mathbf{D}_1(A) = (D_{x1}(A), D_{y1}(A))$ and $\mathbf{D}_2(A) = (D_{x2}(A), D_{y2}(A))$, the electric fluxes at A from different media, as well as the relation between $\mathbf{E}_1(A) = (E_{x1}(A), E_{y1}(A))$ and $\mathbf{E}_2(A) = (E_{x2}(A), E_{y2}(A))$.

Suppose $\mathbf{n} = (n_x, n_y)$ is the unit norm vector at A from region 1, then the corresponding tangent unit vector is $\tau = (n_y, -n_x)$. Therefore at point A, we can calculate

E_τ and D_n in different regions as follows.

$$E_{\tau_1} = \mathbf{E}_1 \cdot \tau = E_{x_1} n_y - E_{y_1} n_x \tag{3.13}$$

$$E_{\tau_2} = \mathbf{E}_2 \cdot \tau = E_{x_2} n_y - E_{y_2} n_x \tag{3.14}$$

Meanwhile,

$$D_{n_1} = \epsilon_1 \mathbf{E}_{n_1} = \epsilon_1 E_{x_1} n_x + \epsilon_1 E_{y_1} n_y \tag{3.15}$$

$$D_{n_2} = \epsilon_2 \mathbf{E}_{n_2} = \epsilon_2 E_{x_2} n_x + \epsilon_2 E_{y_2} n_y \tag{3.16}$$

Based on the fact that $E_{\tau_1} = E_{\tau_2}$ and $D_{n_1} = D_{n_2}$, we have

$$\begin{cases} E_{x_1} n_y - E_{y_1} n_x & = E_{x_2} n_y - E_{y_2} n_x \\ \epsilon_1 E_{x_1} n_x + \epsilon_1 E_{y_1} n_y & = \epsilon_2 E_{x_2} n_x + \epsilon_2 E_{y_2} n_y \end{cases}$$

Or

$$\begin{bmatrix} n_y & -n_x \\ \epsilon_1 n_x & \epsilon_1 n_y \end{bmatrix} \begin{bmatrix} E_{x_1} \\ E_{y_1} \end{bmatrix} = \begin{bmatrix} n_y & -n_x \\ \epsilon_2 n_x & \epsilon_2 n_y \end{bmatrix} \begin{bmatrix} E_{x_2} \\ E_{y_2} \end{bmatrix} \tag{3.17}$$

Therefore, we obtain based on $n_x^2 + n_y^2 = 1$:

$$\begin{bmatrix} E_{x_1} \\ E_{y_1} \end{bmatrix} = \begin{bmatrix} n_y & -n_x \\ \epsilon_1 n_x & \epsilon_1 n_y \end{bmatrix}^{-1} \begin{bmatrix} n_y & -n_x \\ \epsilon_2 n_x & \epsilon_2 n_y \end{bmatrix} \begin{bmatrix} E_{x_2} \\ E_{y_2} \end{bmatrix}$$

Or

$$\begin{bmatrix} E_{x_1} \\ E_{y_1} \end{bmatrix} = \begin{bmatrix} \frac{\epsilon_2}{\epsilon_1} n_x^2 + n_y^2 & (\frac{\epsilon_2}{\epsilon_1} - 1) n_x n_y \\ (\frac{\epsilon_2}{\epsilon_1} - 1) n_x n_y & n_x^2 + \frac{\epsilon_2}{\epsilon_1} n_y \end{bmatrix} \begin{bmatrix} E_{x_2} \\ E_{y_2} \end{bmatrix} \tag{3.18}$$

Giving

$$\begin{cases} E_{x_1} &= (\frac{\epsilon_2}{\epsilon_1} n_x^2 + n_y^2) E_{x_2} + (\frac{\epsilon_2}{\epsilon_1} - 1) n_x n_y E_{y_2} \\ E_{y_1} &= (\frac{\epsilon_2}{\epsilon_1} - 1) n_x n_y E_{x_2} + (n_x^2 + \frac{\epsilon_2}{\epsilon_1} n_y^2) E_{y_2} \end{cases} \tag{3.19}$$

Furthermore, by using $\mathbf{D}_i = \epsilon_i \mathbf{E}_i$ at A, we obtain easily,

$$\begin{cases} D_{x_1} &= (\frac{\epsilon_1}{\epsilon_2} n_y^2 + n_x^2) D_{x_2} + (1 - \frac{\epsilon_1}{\epsilon_2}) n_x n_y D_{y_2} \\ D_{y_1} &= (1 - \frac{\epsilon_1}{\epsilon_2}) n_x n_y D_{x_2} + (\frac{\epsilon_1}{\epsilon_2} n_x^2 + n_y^2) D_{y_2} \end{cases} \tag{3.20}$$

If the interface Γ is parallel or orthogonal to x-axis, either $n_y = 0$ or $n_x = 0$ so $n_x \cdot n_y = 0$. Then the relation (3.19) involving $\mathbf{E}_1$ and $\mathbf{E}_2$ will be simplified such that E_{x_1} and E_{y_1} will only depend on E_{x_2} or E_{y_2} respectively. Same holds for $\mathbf{D}_1$ and $\mathbf{D}_2$ in relation (3.20).

By using (3.20), we can express D_{x_2} in region 2 based on its neighbor D_{x_1} in region 1 and its corresponding D_{y_2} in the same region 2. Similar formula can also be derived for D_{y_2} based on D_{y_1} and D_{x_2}.

$$D_{x_2} = \frac{\epsilon_2}{\epsilon_2 n_x^2 + \epsilon_1 n_y^2} D_{x_1} + \frac{(\epsilon_1 - \epsilon_2) n_x n_y}{\epsilon_2 n_x^2 + \epsilon_1 n_y^2} D_{y_2} \tag{3.21}$$

$$D_{y_2} = \frac{(\epsilon_1 - \epsilon_2) n_x n_y}{\epsilon_1 n_x^2 + \epsilon_2 n_y^2} D_{x_2} + \frac{\epsilon_2}{\epsilon_1 n_x^2 + \epsilon_2 n_y^2} D_{y_1} \tag{3.22}$$

(3.19) will be used to derive the new second-order scheme for Faraday's law while

(3.21) and (3.22) will be used to derive the new second-order scheme for Ampere's law in the next section.

3.3 Second-order FDTD Scheme in Nonuniform Media

In this section we consider a domain composed of two different media with relative permittivities ϵ_1 and ϵ_2. The standard second order FDTD scheme (3.7) (3.11) (3.12) will not work around the interface between these two media where the rectangle S in (3.1) and (3.2) intersects with both media. We need to construct new FDTD schemes around the interface based on Section 3.2.

First let's discretize Faraday's law (3.1) around the interface Γ.

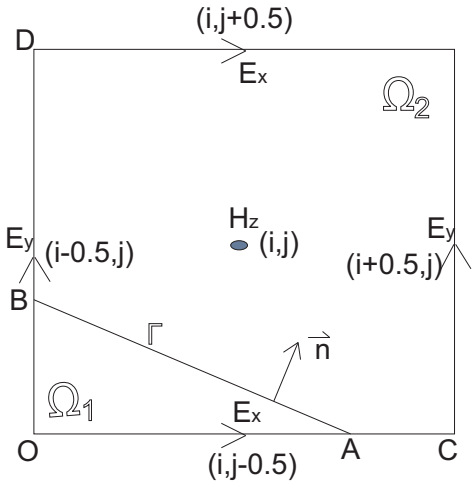

Figure 3.5: Discretization of Faraday's law across Γ

As in Section 3.1, we choose S to be the rectangle centered at (i, j). If the interface Γ between media Ω_1 and Ω_2 does not cut through interior of S, the standard scheme (3.7) still applies here. Therefore, we only need to consider the case where Γ intersects with S.

It's obvious that Γ will only intersect with at most two sides, e.g. the bottom and left side as in Figure 3.5. All other cases can be handled in the same way.

Discretization of the left hand side term of (3.1) at the time t_N via finite difference scheme yields

$$\frac{\iint_S \mathbf{H}^{n+\frac{1}{2}} \cdot \mathbf{n} dS - \iint_S \mathbf{H}^{n-\frac{1}{2}} \cdot \mathbf{n} dS}{\Delta t} = -\oint_{\partial S} \mathbf{E}^n \cdot d\mathbf{l} + \mathcal{O}(\Delta t \Delta x \Delta y)$$

or

$$\iint_S \mathbf{H}^{n+\frac{1}{2}} \cdot \mathbf{n} dS = \iint_S \mathbf{H}^{n-\frac{1}{2}} \cdot \mathbf{n} dS - \Delta t \oint_{\partial S} \mathbf{E}^n \cdot d\mathbf{l} + \mathcal{O}(\Delta t^2 \Delta x \Delta y) \tag{3.23}$$

since $\mathbf{H}$ is always perpendicular to the incident xy-plane and so is always continuous across the interface, then by using midpoint rule,

$$\iint_S \mathbf{H}^{n+\frac{1}{2}} \cdot \mathbf{n} dS = \mathbf{H}^{n+\frac{1}{2}}_{z_{(i,j)}} \Delta x \Delta y + \mathcal{O}(\Delta x^3 \Delta y) \tag{3.24}$$

$$\iint_S \mathbf{H}^{n-\frac{1}{2}} \cdot \mathbf{n} dS = \mathbf{H}^{n-\frac{1}{2}}_{z_{(i,j)}} \Delta x \Delta y + \mathcal{O}(\Delta x^3 \Delta y) \tag{3.25}$$

However the situation for $\mathbf{E}$ is much more complicated. In Figure 3.5 the line integral of $\mathbf{E}^n$ along the right and top sides can be handled as in Section 3.1 since they are completely inside Ω_2. But the line integrals along the bottom and left sides need to be handled separately.

$$\begin{aligned}
\oint_{\partial S} \mathbf{E}^n \cdot d\mathbf{l} &= \int_{bottom} \mathbf{E}^n \cdot d\mathbf{l} + \int_{left} \mathbf{E}^n \cdot d\mathbf{l} \\
&\quad + \int_{(j-\frac{1}{2})\Delta y}^{(j+\frac{1}{2})\Delta y} E^n_{(i+\frac{1}{2},y)} dy - \int_{(i-\frac{1}{2})\Delta x}^{(i+\frac{1}{2})\Delta x} E^n_{(x,j+\frac{1}{2})} dx \\
&= \int_O^C E^n_{(x,j-\frac{1}{2})} dx - \int_O^D E^n_{(i-\frac{1}{2},y)} dy + E^n_{y_{(i+\frac{1}{2},j)}} \Delta y - E^n_{x_{(i,j+\frac{1}{2})}} \Delta x \\
&\quad + \mathcal{O}(\Delta x^3) + \mathcal{O}(\Delta y^3)
\end{aligned} \tag{3.26}$$

Suppose the portion OA of the bottom side in Ω_1 has length d, and the portion OB of the left side in Ω_1 has length f as in Figure 3.5, then the first two terms on the right hand side of (3.26) can be handled as below:

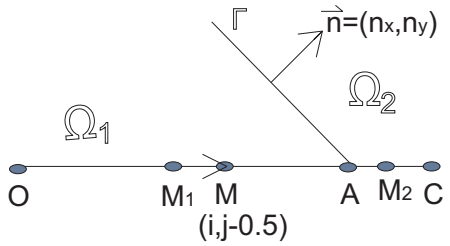

Figure 3.6: Discretization of the integral along bottom side OC

Let's calculate the first term on the right hand side of (3.26), as shown in Figure 3.6 where M, M_1, M_2 are the midpoints of OC (bottom side), OA and AC. Then by applying the integration midpoint rule and Taylor expansion, we obtain

$$\begin{aligned}\int_O^C E^n_{(x,j-\frac{1}{2})}dx &= \int_O^A E^n_{(x,j-\frac{1}{2})}dx + \int_A^C E^n_{(x,j-\frac{1}{2})}dx \\ &= E^n_x|_{M_1}\cdot d + \mathcal{O}(\Delta x^3) + E^n_x|_{M_2}\cdot(\Delta x - d) + \mathcal{O}(\Delta x^3) \\ &= E^n_x|_M \cdot d + E^n_x|_{A,\Omega_2}\cdot(\Delta x - d) + \mathcal{O}(\Delta x^3) \end{aligned} \tag{3.27}$$

By using formula (3.19) with Ω_1 and Ω_2 interchanged, we have

$$E^n_x|_{A,\Omega_2} = (\tfrac{\epsilon_1}{\epsilon_2}n_x^2 + n_y^2)E^n_x|_{A,\Omega_1} + (\tfrac{\epsilon_1}{\epsilon_2} - 1)n_x n_y E^n_y|_{A,\Omega_1} \tag{3.28}$$

Putting it into (3.27) and applying Taylor expansion again yields

$$\begin{aligned}\int_O^C E^n_{(x,j-\frac{1}{2})}dx &= E^n_x|_M \cdot d + (\tfrac{\epsilon_1}{\epsilon_2}n_x^2 + n_y^2)(\Delta x - d)E^n_x|_{A,\Omega_1} \\ &\quad + (\tfrac{\epsilon_1}{\epsilon_2} - 1)n_x n_y(\Delta x - d)E^n_y|_{A,\Omega_1} + \mathcal{O}(\Delta x^3) \\ &= [d + (\Delta x - d)(\tfrac{\epsilon_1}{\epsilon_2}n_x^2 + n_y^2)]E^n_{x_{(i,j-\frac{1}{2})}} \\ &\quad + (\tfrac{\epsilon_1}{\epsilon_2} - 1)n_x n_y(\Delta x - d)E^n_{y_{(i-\frac{1}{2},j-1)}} + \mathcal{O}(\Delta x^3) \qquad (3.29)\end{aligned}$$

where $E^n_{x_{(i,j-\frac{1}{2})}} = E^n_{x_{(M)}}$ for the first term, $E^n_{y_{(i-\frac{1}{2},j-1)}}$ is the value of E^n_y located at point $(i-\frac{1}{2}, j-1)$, which is the closest E_y node to $M = (i, j-\frac{1}{2})$ within Ω_1.

Similarly we can calculate the second term on the right hand side of (3.26). Since the E_y node $(i-\frac{1}{2}, j)$ is located within Ω_2 instead of Ω_1, so the new $\mathbf{n}$ should be negative of old $\mathbf{n}$ used above. Therefore we apply integration midpoint rule, Taylor expansion and formula (3.19) where (n_x, n_y) replaced by $(-n_x, -n_y)$ and ϵ_1, ϵ_2 interchanged, we have

$$\begin{aligned}\int_O^D E^n_{(i-\frac{1}{2},y)}dy &= [f(n_x^2 + \tfrac{\epsilon_2}{\epsilon_1}n_y^2) + (\Delta y - f)]E^n_{y_{(i-\frac{1}{2},j)}} \\ &\quad + (\frac{\epsilon_2}{\epsilon_1} - 1)n_x n_y f E^n_{x_{(i,j+\frac{1}{2})}} + \mathcal{O}(\Delta y^3) \qquad (3.30)\end{aligned}$$

when $E^n_{x_{(i,j+\frac{1}{2})}}$ is the value of E^n_x located at point $(i, j+\frac{1}{2})$ which is the closest E_x node to $(i-\frac{1}{2}, j)$ within Ω_2. By putting (3.29), (3.30) into (3.26), we get

$$\begin{aligned}\oint_{\partial S} \mathbf{E}^n \cdot d\mathbf{l} &= [d + (\Delta x - d)(\tfrac{\epsilon_1}{\epsilon_2}n_x^2 + n_y^2)]E^n_{x_{(i,j-\frac{1}{2})}} + E^n_{y_{(i+\frac{1}{2},j)}}\Delta y - E^n_{x_{(i,j+\frac{1}{2})}}\Delta x \\ &\quad - [f(n_x^2 + \tfrac{\epsilon_2}{\epsilon_1}n_y^2) + (\Delta y - f)]E^n_{y_{(i-\frac{1}{2},j)}} + (\tfrac{\epsilon_1}{\epsilon_2} - 1)n_x n_y(\Delta x - d)E^n_{y_{(i-\frac{1}{2},j-1)}} \\ &\quad - (\tfrac{\epsilon_2}{\epsilon_1} - 1)n_x n_y f E^n_{x_{(i,j+\frac{1}{2})}} + \mathcal{O}(\Delta x^3) + \mathcal{O}(\Delta y^3) \qquad (3.31)\end{aligned}$$

Finally by putting (3.25), (3.26) and (3.31) into (3.23) and dividing both sides by $\Delta x \Delta y$, we obtain the new second-order discretization of Faraday's law:

$$\begin{aligned} H_{z_{(i,j)}}^{n+\frac{1}{2}} = H_{z_{(i,j)}}^{n-\frac{1}{2}} - \tfrac{\Delta t}{\Delta x \Delta y}\{[d + (\Delta x - d)(\tfrac{\epsilon_1}{\epsilon_2} n_x^2 + n_y^2)] E^n_{x_{(i,j-\frac{1}{2})}} + E^n_{y_{(i+\frac{1}{2},j)}} \Delta y \\ - E^n_{x_{(i,j+\frac{1}{2})}} \Delta x - [f(n_x^2 + \tfrac{\epsilon_2}{\epsilon_1} n_y^2) + (\Delta y - f)] E^n_{y_{(i-\frac{1}{2},j)}} \\ + (\tfrac{\epsilon_1}{\epsilon_2} - 1) n_x n_y (\Delta x - d) E^n_{y_{(i-\frac{1}{2},j-1)}} - (\tfrac{\epsilon_2}{\epsilon_1} - 1) n_x n_y f E^n_{x_{(i,j+\frac{1}{2})}} \} \\ + \mathcal{O}(\Delta x^2) + \mathcal{O}(\Delta y^2) + \mathcal{O}(\Delta t^2) \end{aligned} \tag{3.32}$$

It should be noted that the last two terms on the right hand side of (3.32) have been ignored by CP-EP algorithm but they provide necessary corrections for the interface conditions across multiple media. The numerical tests have verify that in order to make the algorithm for Faraday's Law more accurate, instead of using the nearest neighbor $E^n_{y_{(i-\frac{1}{2},j-1)}}$ for the E_x integral along the side OC, we can choose either the average of $E^n_{y_{(i-\frac{1}{2},j-1)}}$ and $E^n_{y_{(i+\frac{1}{2},j)}}$ (if they are both located in Ω_1) or the average of $E^n_{y_{(i+\frac{1}{2},j-1)}}$ and $E^n_{y_{(i-\frac{1}{2},j)}}$ (if they are both located in Ω_1) to replace $E^n_{y_{(i-\frac{1}{2},j-1)}}$ in (3.32) if possible since the midpoint of the above two pairs are more closer to the intersection A on OC than the nearest E_y neighbor $(i - \frac{1}{2}, j - 1)$. Similar trick can also be applied to replace the nearest E_x node $(i, j + \frac{1}{2})$ in Ω_2 for the E_y integral along the side OD if possible.

Next, let us discretize Ampere's law (3.2) around the interface Γ to update E_x^n and E_y^n

To update E_x, we still choose S in (3.2) to be the rectangle in yz-plane whose projection in xy-place is the line segment OC as in Section 3.2. Suppose the interface Γ intersect OC at point A and $OA = f$ as in Figure 3.7. Applying time discretization

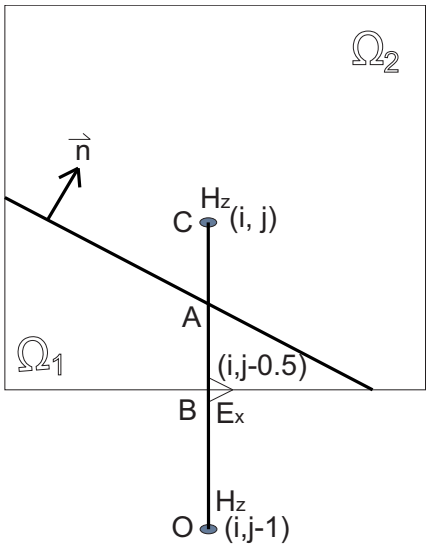

Figure 3.7: Discretization of Ampere's law across Γ

to Ampere's law along S at time $t_{n+\frac{1}{2}}$ yields

$$\frac{\int_O^C D^{n+1}_{x_{(i,y)}}dy - \int_O^C D^{n}_{x_{(i,y)}}dy}{\Delta t} = H^{n+\frac{1}{2}}_{z_{(i,j)}} - H^{n+\frac{1}{2}}_{z_{(i,j-1)}} + \mathcal{O}(\Delta t \Delta y) \tag{3.33}$$

Repeat the same procedure as for Faraday's law while based on formula (3.21), we can compute the integrals of left hand side as follows.

$$\begin{aligned}
\int_O^C D^{n+1}_{x_{(i,y)}}dy &= \int_O^A D^{n+1}_{x_{(i,y)}}dy + \int_A^C D^{n+1}_{x_{(i,y)}}dy \\
&= f D^{n+1}_{x_{(i,j-\frac{1}{2})}} + (\Delta y - f) D^{n+1}_{x_{(A,\Omega_2)}} + \mathcal{O}(\Delta y^3) \\
&= f D^{n+1}_{x_{(i,j-\frac{1}{2})}} + (\Delta y - f)\left[\frac{\epsilon_2}{\epsilon_2 n_x^2 + \epsilon_1 n_y^2} D^{n+1}_{x_{(A,\Omega_1)}} + \frac{(\epsilon_1 - \epsilon_2) n_x n_y}{\epsilon_2 n_x^2 + \epsilon_1 n_y^2} D^{n+1}_{y_{(A,\Omega_2)}}\right] \\
&\quad + \mathcal{O}(\Delta y^3) \\
&= \frac{f(\epsilon_2 n_x^2 + \epsilon_1 n_y^2) + (\Delta y - f)\epsilon_2}{\epsilon_2 n_x^2 + \epsilon_1 n_y^2} D^{n+1}_{x_{(i,j-\frac{1}{2})}} + \frac{(\epsilon_1 - \epsilon_2) n_x n_y}{\epsilon_2 n_x^2 + \epsilon_1 n_y^2}(\Delta y - f) D^{n+1}_{y_{(C)}} \\
&\quad + \mathcal{O}(\Delta y^3)
\end{aligned} \tag{3.34}$$

Similarly,

$$\int_O^C D^n_{x(i,y)}dy = \frac{f(\epsilon_2 n_x^2+\epsilon_1 n_y^2)+(\Delta y-f)\epsilon_2}{\epsilon_2 n_x^2+\epsilon_1 n_y^2} D^n_{x_{(i,j-\frac{1}{2})}} + \frac{(\epsilon_1-\epsilon_2)n_x n_y}{\epsilon_2 n_x^2+\epsilon_1 n_y^2}(\Delta y-f)D^n_{y_{(C)}} + \mathcal{O}(\Delta y^3) \tag{3.35}$$

Furthermore,

$$\begin{aligned} D^{n+1}_{y_{(C)}} &= D^n_{y_{(C)}} + \frac{\partial D_y}{\partial t}|_C^{t_n}\cdot\Delta t + \mathcal{O}(\Delta t^2) \\ &= D^n_{y_{(C)}} - \frac{\partial H_z}{\partial x}|_C^{t_{n+\frac{1}{2}}}\cdot\Delta t + \mathcal{O}(\Delta t^2) \\ &= D^n_{y_{(C)}} - \left(\frac{H^{n+\frac{1}{2}}_{z_{(i+1,j)}} - H^{n+\frac{1}{2}}_{z_{(i,j)}}}{\Delta x}\right)\Delta t + \mathcal{O}(\Delta t\Delta x) + \mathcal{O}(\Delta t^2) \end{aligned} \tag{3.36}$$

By putting (3.34), (3.35) and (3.36) into (3.33), we obtain

$$\begin{aligned} &\frac{f(\epsilon_2 n_x^2+\epsilon_1 n_y^2)+(\Delta y-f)\epsilon_2}{\epsilon_2 n_x^2+\epsilon_1 n_y^2}\left(D^{n+1}_{x_{(i,j-\frac{1}{2})}} - D^n_{x_{(i,j-\frac{1}{2})}}\right) = \Delta t\left(H^{n+\frac{1}{2}}_{z_{(i,j)}} - H^{n+\frac{1}{2}}_{z_{(i,j-1)}}\right) \\ &+\frac{\Delta t}{\Delta x}\frac{(\epsilon_1-\epsilon_2)n_x n_y}{\epsilon_2 n_x^2+\epsilon_1 n_y^2}(\Delta y-f)\left(H^{n+\frac{1}{2}}_{z_{(i+1,j)}} - H^{n+\frac{1}{2}}_{z_{(i,j)}}\right) + \mathcal{O}(\Delta t^2\Delta x) + \mathcal{O}(\Delta y^3) + \mathcal{O}(\Delta t^3) \end{aligned} \tag{3.37}$$

which, based on $D_x = \epsilon_1 E_x$ in Ω_1, becomes

$$\begin{aligned} E^{n+1}_{x_{(i,j-\frac{1}{2})}} &= E^n_{x_{(i,j-\frac{1}{2})}} + \Delta t\frac{\frac{\epsilon_2}{\epsilon_1}n_x^2+n_y^2}{f(\epsilon_2 n_x^2+\epsilon_1 n_y^2)+(\Delta y-f)\epsilon_2}\left(H^{n+\frac{1}{2}}_{z_{(i,j)}} - H^{n+\frac{1}{2}}_{z_{(i,j-1)}}\right) \\ &+ \frac{\Delta t}{\Delta x}\frac{(\Delta y-f)(1-\frac{\epsilon_2}{\epsilon_1})n_x n_y}{f(\epsilon_2 n_x^2+\epsilon_1 n_y^2)+(\Delta y-f)\epsilon_2}\left(H^{n+\frac{1}{2}}_{z_{(i+1,j)}} - H^{n+\frac{1}{2}}_{z_{(i,j)}}\right) \\ &+ \mathcal{O}(\Delta x^2) + \mathcal{O}(\Delta y^2) + \mathcal{O}(\Delta t^2) \end{aligned} \tag{3.38}$$

Which shows second-order discretization of Ampere's law for updating E_x.

It should also be noted that the last term on the right hand side of (3.38) have been

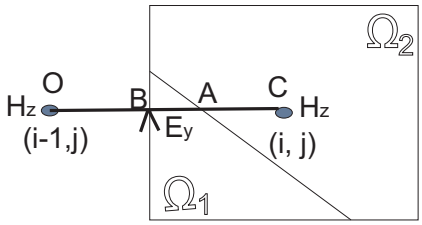

Figure 3.8: Discretization of the integral along OC

ignored by CP-EP algorithm but it provides necessary corrections for the interface conditions across multiple media. The numerical tests have also verified that in order to make the algorithm for Ampere's Law more accurate, these two H_z values in the last term should stay close to the interface. That is, if the normal direction of the interface n satisfies $n_x \cdot n_y > 0$ as shown in Figure 3.7, we need to use $(H^{n+\frac{1}{2}}_{z_{(i,j)}} - H^{n+\frac{1}{2}}_{z_{(i-1,j)}})$ to replace the H_z part of the last term since these two H_z points are closer to the interface than the original terms, while for $n_x \cdot n_y \leq 0$ case, (3.38) can remain unchanged since their two H_z nodes are already closer to the interface than other pairs. This improvement is feasible since H_z in continuous in the whole domain. Same trick can also be applied to the updating of E_y shown below.

Similarly, update of E_y at point $B = (i - \frac{1}{2}, j)$ by Ampere's law (3.2) can be taken care analogously as shown in Figure 3.8, Where the interface Γ intersects the line segment OC, projection of S at xy-plane, at A. Let $OA = d$. By repeating the same procedure as above while based on formula (3.22), we can also obtain the second-order discretization of Ampere's law for E_y as below:

$$\begin{aligned} E^{n+1}_{y_{(i,j-\frac{1}{2})}} &= E^{n}_{y_{(i,j-\frac{1}{2})}} + \Delta t \frac{\frac{\epsilon_2}{\epsilon_1} n_y^2 + n_x^2}{d(\epsilon_1 n_x^2 + \epsilon_2 n_y^2) + (\Delta x - d)\epsilon_2} \left(H^{n+\frac{1}{2}}_{z_{(i-1,j)}} - H^{n+\frac{1}{2}}_{z_{(i,j)}} \right) \\ &+ \frac{\Delta t}{\Delta y} \frac{(\Delta x - d)(1 - \frac{\epsilon_2}{\epsilon_1}) n_x n_y}{d(\epsilon_1 n_x^2 + \epsilon_2 n_y^2) + (\Delta x - d)\epsilon_2} \left(H^{n+\frac{1}{2}}_{z_{(i,j)}} - H^{n+\frac{1}{2}}_{z_{(i,j+1)}} \right) \\ &+ \mathcal{O}(\Delta x^2) + \mathcal{O}(\Delta y^2) + \mathcal{O}(\Delta t^2) \end{aligned} \tag{3.39}$$

Compared with standard FDTD algorithm (3.7), (3.11) and (3.12) which only shows second-order convergence within a uniform medium, our new algorithm (3.32), (3.38) and (3.39) can still achieve second-order convergence in a non-uniform domain where the orientation of the interface between these two media is arbitrary.

3.4 Second-order FDTD Scheme Reduction to Know Results

In this section, we consider a special case where the interface Γ is parallel with horizontal x-axis, shown in Figure 3.9. We want to demonstrate that our new algorithm reduces to the established second-order FDTD algorithm for horizontal or vertical interface with respect to Cartesian Coordinates reported in [10]. Therefore, our new algorithm can be regarded as the generalization of established second-order algorithm for any oriented interface.

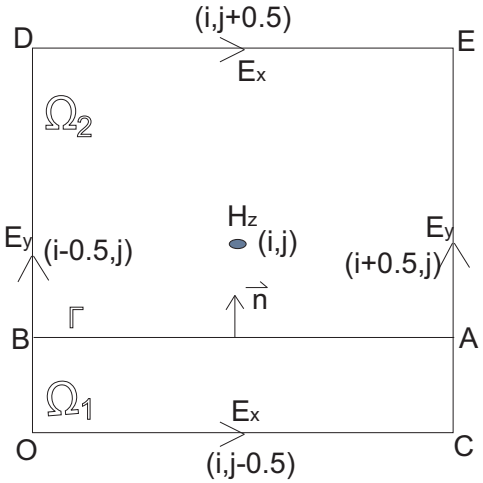

Figure 3.9: Second-order scheme for a horizontal interface

First let's discretize Faraday's law (3.1) by choosing S to be the rectangle centered at (i, j) where the interface Γ intersect two vertical sides OD and CE at point B and

A, respectively. By using the same integration technique as in Section 3.3. we obtain.

$$H^{n+\frac{1}{2}}_{z_{(i,j)}}\Delta x\Delta y = H^{n-\frac{1}{2}}_{z_{(i,j)}}\Delta x\Delta y - \Delta t \oint_{\partial S} E^n \cdot dl + \mathcal{O}(\Delta t^2\Delta x\Delta y) + \mathcal{O}(\Delta x^3\Delta y) \quad (3.40)$$

where

$$\begin{aligned}\oint_{\partial S} E^n dl &= \oint_O^C E^n dl + \oint_C^E E^n dl + \oint_E^D E^n dl + \oint_D^O E^n dl \\ &= E^n_{x_{(i,j-\frac{1}{2})}}\Delta x + \int_{(j-\frac{1}{2})\Delta y}^{(j+\frac{1}{2})\Delta y} E^n_{(i+\frac{1}{2},y)}dy - E^n_{x_{(i,j+\frac{1}{2})}}\Delta x \\ &- \int_{(j-\frac{1}{2})\Delta y}^{(j+\frac{1}{2})\Delta y} E^n_{(i-\frac{1}{2},y)}dy + \mathcal{O}(\Delta x^3) \end{aligned} \quad (3.41)$$

Next let's deal with the second and fourth terms on the right hand side of (3.41) based on relation of $E(x,y)$ across Γ, (3.15) in Sec 3.2. Let $OB = AC = f$, then $BD = AE = \Delta y - f$, since $\mathbf{n} = (0,1)$ along Γ, we have the second term

$$\begin{aligned}\int_{(j-\frac{1}{2})\Delta y}^{(j+\frac{1}{2})\Delta y} E^n_{(i+\frac{1}{2},y)}dy &= \int_C^A E^n_{(i+\frac{1}{2},y)}dy + \int_A^E E^n_{(i+\frac{1}{2},y)}dy \\ &= E^n_{y_1,A}f + E^n_{y_{(i+\frac{1}{2},j)}}(\Delta y - f) + \mathcal{O}(\Delta y^3) \\ &= \tfrac{\epsilon_2}{\epsilon_1}E^n_{y_2,A}f + E^n_{y_{(i+\frac{1}{2},j)}}(\Delta y - f) + \mathcal{O}(\Delta y^3) \\ &= \tfrac{\epsilon_2}{\epsilon_1}E^n_{y_{(i+\frac{1}{2},j)}}f + E^n_{y_{(i+\frac{1}{2},j)}}(\Delta y - f) + \mathcal{O}(\Delta y^3) \\ &= [\tfrac{\epsilon_2}{\epsilon_1}f + (\Delta y - f)]E^n_{y_{(i+\frac{1}{2},j)}} + \mathcal{O}(\Delta y^3) \end{aligned} \quad (3.42)$$

Similarly, the fourth term

$$\int_{(j-\frac{1}{2})\Delta y}^{(j+\frac{1}{2})\Delta y} E^n_{(i-\frac{1}{2},y)}dy = [\tfrac{\epsilon_2}{\epsilon_1}f + (\Delta y - f)]E^n_{y_{(i-\frac{1}{2},j)}} + \mathcal{O}(\Delta y^3) \quad (3.43)$$

putting (3.42) and (3.43) into (3.41), we get

$$\oint_{\partial S} E^n dl = \left[E^n_{x_{(i,j-\frac{1}{2})}} - E^n_{x_{(i,j+\frac{1}{2})}}\right]\Delta x + \left[E^n_{y_{(i+\frac{1}{2},j)}} - E^n_{y_{(i-\frac{1}{2},j)}}\right]\left[\tfrac{\epsilon_2}{\epsilon_1} f + (\Delta y - f)\right] + \mathcal{O}(\Delta x^3) + \mathcal{O}(\Delta y^3) \tag{3.44}$$

putting (3.44) into (3.40) and dividing both sides by $\Delta x \Delta y$ we obtain

$$H^{n+\frac{1}{2}}_{z_{(i,j)}} = H^{n-\frac{1}{2}}_{z_{(i,j)}} - \Delta t \left[\frac{E^n_{x_{(i,j-\frac{1}{2})}} - E^n_{x_{(i,j+\frac{1}{2})}}}{\Delta y} + \frac{E^n_{y_{(i+\frac{1}{2},j)}} - E^n_{y_{(i-\frac{1}{2},j)}}}{\Delta x} \cdot \left(\frac{\epsilon_2}{\epsilon_1}\frac{f}{\Delta y} + \left(1 - \frac{f}{\Delta y}\right)\right)\right] + \mathcal{O}(\Delta t^2) + \mathcal{O}(\Delta x^2) + \mathcal{O}(\Delta y^2) \tag{3.45}$$

If we define ϵ^*_{12} by $\frac{1}{\epsilon^*_{12}} = \frac{\frac{f}{\Delta y}}{\epsilon_1} + \frac{1-\frac{f}{\Delta y}}{\epsilon_2}$, then ϵ^*_{12} means the harmonic mean of permittivity along normal direction, and the above equation is equivalent to

$$H^{n+\frac{1}{2}}_{z_{(i,j)}} = H^{n-\frac{1}{2}}_{z_{(i,j)}} - \Delta t \left[\frac{D^n_{x_{(i,j-\frac{1}{2},j)}} \cdot \frac{1}{\epsilon_1} - D^n_{x_{(i,j+\frac{1}{2})}} \cdot \frac{1}{\epsilon_2}}{\Delta y} + \frac{D^n_{y_{(i+\frac{1}{2},j)}} \cdot \frac{1}{\epsilon^*_{12}} - D^n_{y_{(i-\frac{1}{2},j)}} \cdot \frac{1}{\epsilon^*_{12}}}{\Delta x}\right] + \mathcal{O}(\Delta t^2) + \mathcal{O}(\Delta x^2) + \mathcal{O}(\Delta y^2) \tag{3.46}$$

which verifies second-order convergence of FDTD along horizontal interface if the harmonic mean ϵ^*_{12} is chosen as the mean of normal permittivity, as reported in [10]. Next let us discretize Ampere's law (3.2) to update E^n_x and E^n_y with the same procedure in Section 3.3. To update E^n_x at $(i, j-\frac{1}{2})$, the surface S will intersect xy-plane with the line segment from node $(i, j-1)$ to node (i, j). Therefore, the bottom portion of the segment with length $(\frac{\Delta y}{2} + f)$ is located in Ω_1, while the top portion with length $(\frac{\Delta y}{2} - f)$ is located in Ω_2. Apply the time discretization and integration

technique to (3.2), we have

$$\int_{(j-1)\Delta y}^{(j-1)\Delta y+(\frac{\Delta y}{2}+f)} D^{n+1}_{x_{(i,y)}}dy + \int_{(j-1)\Delta y+(\frac{\Delta y}{2}+f)}^{j\cdot\Delta y} D^{n+1}_{x_{(i,y)}}dy = \int_{(j-1)\Delta y}^{(j-1)\Delta y+(\frac{\Delta y}{2}+f)} D^{n}_{x_{(i,y)}}dy$$

$$+\int_{(j-1)\Delta y+(\frac{\Delta y}{2}+f)}^{j\cdot\Delta y} D^{n+1}_{x_{(i,y)}}dy + \Delta t\left(H^{n+\frac{1}{2}}_{z_{(i,j)}} - H^{n+\frac{1}{2}}_{z_{(i,j-1)}}\right) + \mathcal{O}(\Delta t^2\Delta y) \tag{3.47}$$

Applying relation of $D(x,y)$ across Γ, (3.20) in Section 3.2. to the second term on both sides yields

$$D^{n+1}_{x_{(i,j-\frac{1}{2})}}(\tfrac{\Delta y}{2}+f) + D^{n+1}_{x_{(i,j-\frac{1}{2})}}\tfrac{\epsilon_2}{\epsilon_1}(\tfrac{\Delta y}{2}-f) = D^{n}_{x_{(i,j-\frac{1}{2})}}(\tfrac{\Delta y}{2}+f)$$

$$+D^{n}_{x_{(i,j)}}\tfrac{\epsilon_2}{\epsilon_1}(\Delta y - f) + \Delta t\left(H^{n+\frac{1}{2}}_{z_{(i,j)}} - H^{n+\frac{1}{2}}_{z_{(i,j-1)}}\right) + \mathcal{O}(\Delta t^2\Delta y) + \mathcal{O}(\Delta y^3) \tag{3.48}$$

since $D_x = \epsilon_1 E_x$ in Ω_1, (3.48) becomes

$$E^{n+1}_{x_{(i,j-\frac{1}{2})}}\left[(\tfrac{\Delta y}{2}+f)\epsilon_1 + (\tfrac{\Delta y}{2}-f)\epsilon_2\right] = E^{n}_{x_{(i,j-\frac{1}{2})}}\left[(\tfrac{\Delta y}{2}+f)\epsilon_1 + (\tfrac{\Delta y}{2}-f)\epsilon_2\right]$$

$$+\Delta t\left(H^{n+\frac{1}{2}}_{z_{(i,j)}} - H^{n+\frac{1}{2}}_{z_{(i,j-1)}}\right) + \mathcal{O}(\Delta t^2\Delta y) + \mathcal{O}(\Delta y^3) \tag{3.49}$$

which can be simplified

$$E^{n+1}_{x_{(i,j-\frac{1}{2})}} = E^{n}_{x_{(i,j-\frac{1}{2})}} + \frac{\Delta t}{(\frac{1}{2}+\frac{f}{\Delta y})\epsilon_1 + (\frac{1}{2}-\frac{f}{\Delta y})\epsilon_2}\frac{(H^{n+\frac{1}{2}}_{z_{(i,j)}} - H^{n+\frac{1}{2}}_{z_{(i,j-1)}})}{\Delta y}$$

$$+\mathcal{O}(\Delta t^2) + \mathcal{O}(\Delta y^2) \tag{3.50}$$

which verifies second-order convergence of FDTD along horizontal interface if $(\frac{1}{2}+\frac{f}{\Delta y})\epsilon_1 + (\frac{1}{2}-\frac{f}{\Delta y})\epsilon_2$ is chosen as the mean of tangential permittivity, as reported in [10]. Since the surface S used to update E^n_y at $(i-\frac{1}{2}, j)$ is located within Ω_2, then

the formula for E_y^n is completely the same as the uniform case, that is,

$$E_{y_{(i-\frac{1}{2},j)}}^{n+1} = E_{y_{(i-\frac{1}{2},j)}}^{n} + \frac{\Delta t}{\epsilon_2} \frac{(H_{z_{(i-1,j)}}^{n+\frac{1}{2}} - H_{z_{(i,j)}}^{n+\frac{1}{2}})}{\Delta x} + \mathcal{O}(\Delta x^2) + \mathcal{O}(\Delta t^2) \tag{3.51}$$

In summary, the computational FDTD scheme (3.45), (3.50), (3.51) recovers the second-order convergence when the interface is parallel with Cartesian coordinates by choosing the mean of permittivity along normal and tangential directions of Γ as reported in [10]. Therefore, our new algorithm is the generalization of the existing second order FDTD scheme for any oriented interface.

Chapter 4

Numerical Results

In this chapter, we will demonstrate convergence order and stability of our new BC-EP algorithm numerically. To accomplish this task, we implement our algorithm to solve the Maxwell's equations on a dielectric cylinder, together with the staircasing, V-EP, and CP-EP methods. All the implementations are set up for the 2D FDTD TE case. The total scattering cross sections (SCS) are calculated by all four methods and then compared with the well-known analytic solution by Mie Theory [3] so as to measure the accuracy of each method.

4.1 Numerical Setup

In this section, we set up the numerical simulation environment for all the numerical tests. Our BC-EP algorithm is implemented as outlined in the previous chapter. The second algorithm that is tested for the same simulation is CP-EP [17]. Since there are various kinds of ways to implement the original staircasing method, we test staircasing as the third method by assigning the effective permittivity for each field component by its location individually. As for the last V-EP method, we use the intercepts of the device boundary with the unit cells to create the approximate volume ratio so as to calculate the effective electric permittivity for the unit cell and assigns that value to all the field components in that cell. Meanwhile, the analytic

solution for the dielectric cylinder in our model is calculated by using the Mie theory in [3].

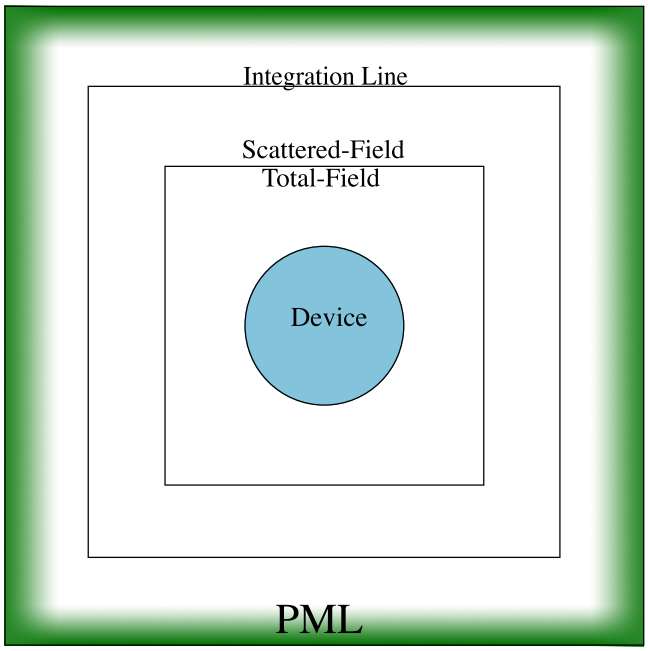

Figure 4.1: The setup of our numerical test using a dielectric cylinder, giving lots of space for the total-field/scattered-field and integration line before the PML

The dielectric cylinder is simulated in an area that is ten times the radius of the cylinder plus some extra space for PML condition. The cylinder is centered at $((\frac{N_x}{2}+0.5)*\Delta x, (\frac{N_y}{2}+0.5)*\Delta y)$ where N_x and N_y are the number of the cells along the x and y directions, Δx and Δy are the horizontal and vertical mesh sizes of each cell as seen in Figure 4.1. We ran our test for two cases: one case for a larger cylinder with radius $r = 400nm$ and another case for a smaller cylinder with $r = 150nm$. The total-field/scattered-field line is three times the length of the cylinder radius r away from the center, and the integration line for calculating SCS is four times r away from the center, while the PML starts at five times r away from the center.

The source wave is a planer wave in the E_y direction with a Gaussian envelope $\exp(\frac{-(t-t_0)^2}{2} * (\frac{1}{\pi*(c/\lambda_0 - c/\lambda_1)*\sqrt{2})^2}) * \cos((2*\pi*c)*t)$, where t_0 is six times Δt, c is speed of light in a vacuum, and $[\lambda_0, \lambda_1]$ is the testing range of wavelengths. In our simulation, we calculate SCS for 601 wavelengths ranging from $\lambda_0 = 400nm$ to $\lambda_1 = 1000nm$ of visual light spectrum with equal distance. Fast Fourier transform (FFT) is then applied to transform the electric and magnetic fields from spatial domain into light frequency domain so as to calculate SCS over all related wavelengths.

We use square unit cells with $\Delta x = \Delta y$ to simplify our simulation. The time step is set to $\Delta t = \frac{S\Delta x}{c}$ where $S = \frac{0.98}{\sqrt{3}}$ to ensure stability [20]. Also for stability concerns, Δx were chosen to divide the smallest tested wave length ($\lambda_0 = 400nm$) by at least twenty times. The total SCS is calculated by using the Poynting Vector along with the integration line as seen in Figure 4.1. Meanwhile, Mie theory is used to calculate the true value of total SCS for each wavelength. The number of iterations for the main FDTD loop is set large enough in order to give enough time for the electric and magnetic waves to leave the simulated area for stable SCS calculation.

4.2 Accuracy and Error Convergence

In this section, we investigate the accuracy and the error convergence order of our new algorithm and compare it with other similar methods. We test all the algorithms for a circular cylinder with radius $r = 400nm$ and permittivity $\epsilon = 3$. The background media ia always set as air with $\epsilon = 1$. The mesh size is originally set to $\Delta x = \Delta y = 10nm$. Each algorithm has been run to calculate the total SCS. This process is then repeated for smaller and smaller mesh sizes. As seen in Figure 4.2, the relative errors between the numerical values from all methods and the true solution are quite small. But we can still see that BC-EP has the smallest error while V-EP has the largest error. Meanwhile, for each mesh size Δx, the average relative error of SCS

is calculated among all the wavelengths for each method. In order to observe the error convergence order clearly, the average relative errors versus the mesh sizes are converted into a log scale where N_λ denotes the log of the number of mesh points for the radius of the cylinder, as seen in Figure 4.3.

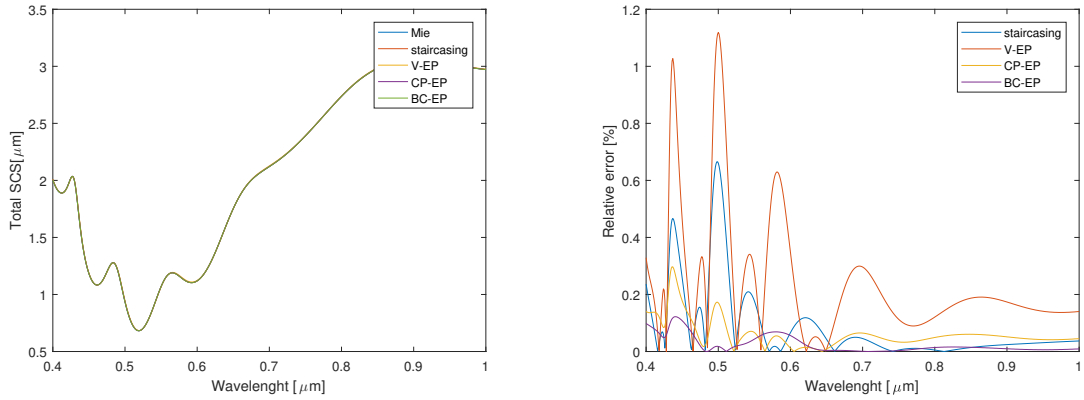

(a) Overall SCS (b) Relative error

Figure 4.2: Total SCS calculation of a cylinder, $\epsilon = 3$ and radius $r = 400nm$. The grid size is $\Delta x = \Delta y = 2.8nm$.

This whole process is then repeated for other larger permittivity values until reaching $\epsilon = 10$. The numerical results are reported in Figure 4.4 and Figure 4.5 for $\epsilon = 6$, and in Figure 4.6 and Figure 4.7 for $\epsilon = 10$. The other ϵ have similar outcomes.

It can be seen that BC-EP gives the least amount of error for most cases, followed by CP-EP. Staircasing results are quite erratic and its error doesn't go down in a uniform manner due to random nature of some mesh sizes conforming with the cylinder better than others. V-EP has the worst error but gives a uniform error decrease with smaller mesh sizes, and therefore gives more consistent results over staircasing.

To further investigate the order of convergence of all the algorithms, we estimate the convergence order by computing the slopes from the log figures for all the given permittivity. Table 4.1 shows that BC-EP algorithm converges significantly

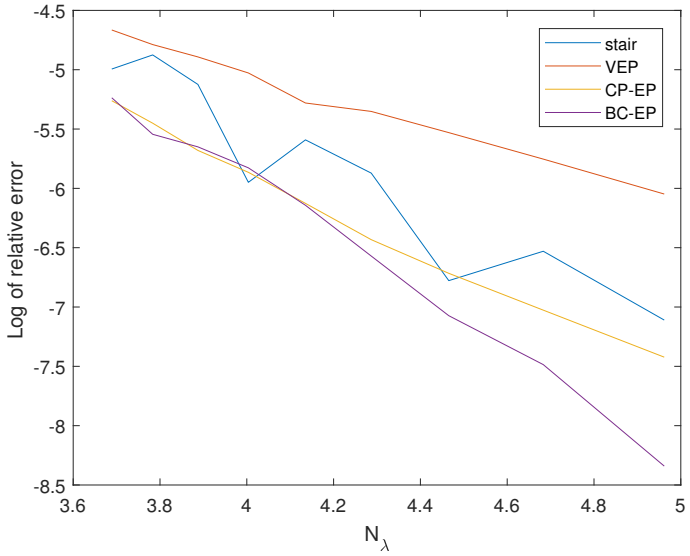

Figure 4.3: The average relative error of a cylinder in log scale, $\epsilon = 3$ and radius $r = 400nm$. $N_\lambda = \log(\frac{400nm}{\Delta x})$.

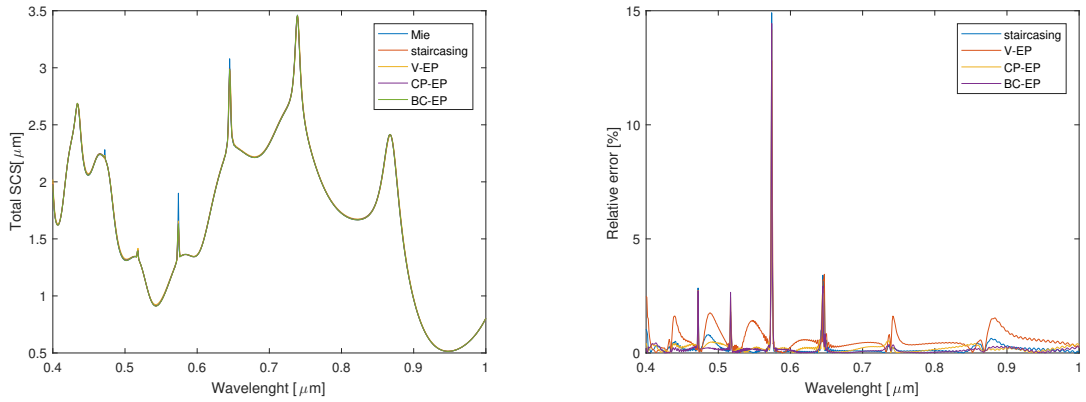

(a) Overall SCS (b) Relative error

Figure 4.4: Total SCS calculation of a cylinder, $\epsilon = 6$ and radius $r = 400nm$. The grid size is $\Delta x = \Delta y = 2.8nm$.

faster than all the other algorithms. In most cases, it approaches second-order as demonstrated theoretically in the previous chapter. CE-EP is the second in terms of convergence order and outperforms both staircasing and V-EP as already reported in the literature [17].

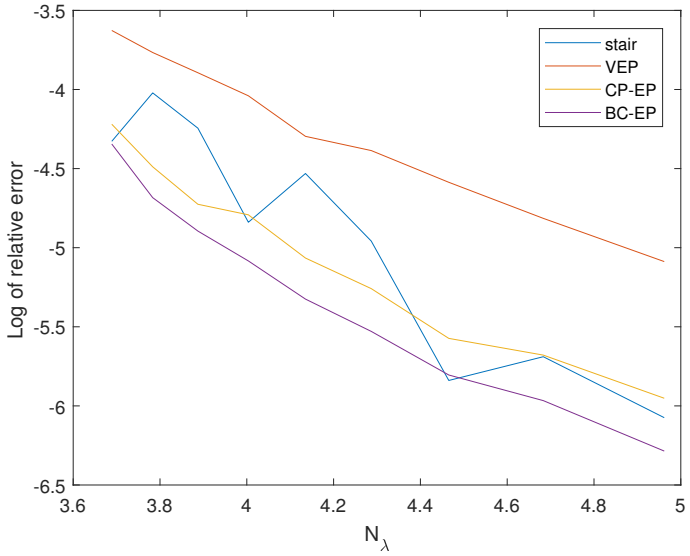

Figure 4.5: The average relative error of a cylinder in log scale, $\epsilon = 6$ and radius $r = 400nm$. $N_\lambda = \log(\frac{400nm}{\Delta x})$.

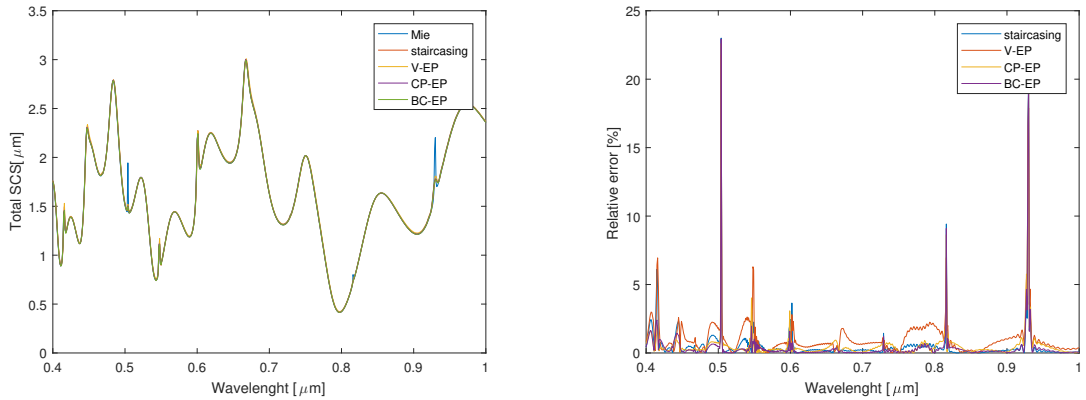

(a) Overall SCS (b) Relative error

Figure 4.6: Total SCS calculation of a cylinder, $\epsilon = 10$ and radius $r = 400nm$. The grid size is $\Delta x = \Delta y = 2.8nm$.

To complete the final evaluation of the performance for all the methods, the whole test suite is then repeated for another circular cylinder with smaller radius $r = 150nm$. All the results are very similar and for brevity, we only report the case of $\epsilon = 6$, as seen in Figure 4.8 and Figure 4.9. It can be seen that the BC-EP algorithm has a higher

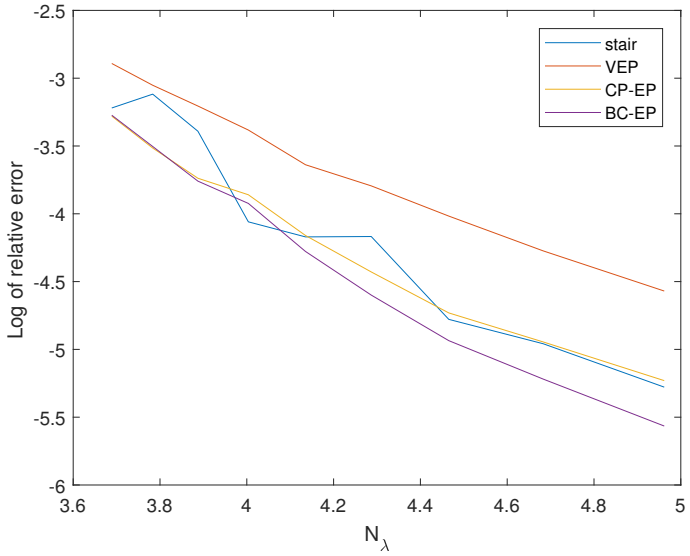

Figure 4.7: The average relative error of a cylinder in log scale, $\epsilon = 10$ and radius $r = 400nm$. $N_\lambda = \log(\frac{400nm}{\Delta x})$.

Permittivity	Staircasing	V-EP	CP-EP	BC-EP
$\epsilon = 3$	1.6621	1.0860	1.6977	2.4386
$\epsilon = 4$	1.0700	1.0850	1.4560	1.9251
$\epsilon = 5$	1.2160	1.1294	1.5267	1.6974
$\epsilon = 6$	1.3723	1.1476	1.3607	1.5247
$\epsilon = 7$	1.4322	1.1834	1.3800	1.6014
$\epsilon = 8$	1.4283	1.1860	1.3564	1.6423
$\epsilon = 9$	1.4867	1.2262	1.4333	1.6837
$\epsilon = 10$	1.6172	1.3183	1.5323	1.8006

Table 4.1: Order of convergence for each FDTD algorithm and for each given permittivity in a cylinder of $r = 400nm$.

convergence order than others. To be more specific, BC-EP, CP-EP, Staircasing and V-EP have the order of convergence 1.4005, 0.92869, 0.92802 and 1.0059, respectively, based on Figure 4.9.

In summary, our new BC-EP algorithm is more accurate and converges faster than all the similar methods reported in the literature.

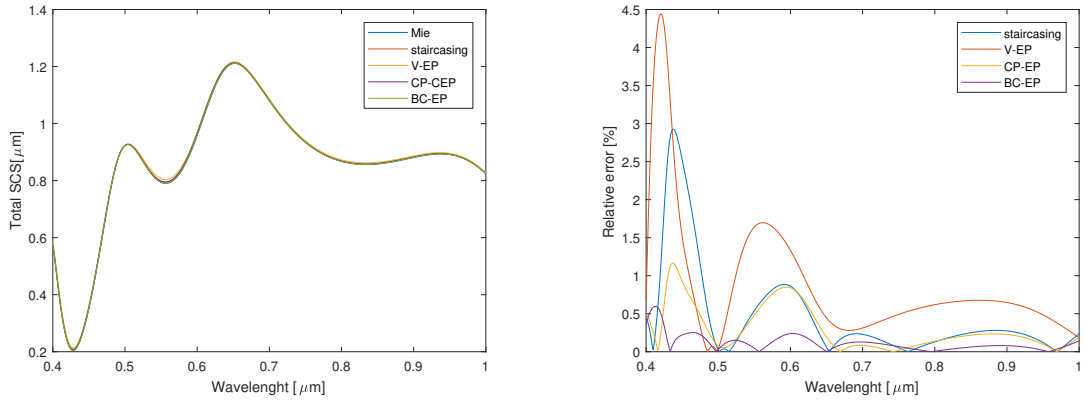

(a) Overall SCS (b) Relative error

Figure 4.8: Total SCS calculation of a cylinder, $\epsilon = 6$ and radius $r = 150nm$. The grid size is $\Delta x = \Delta y = 2.8nm$.

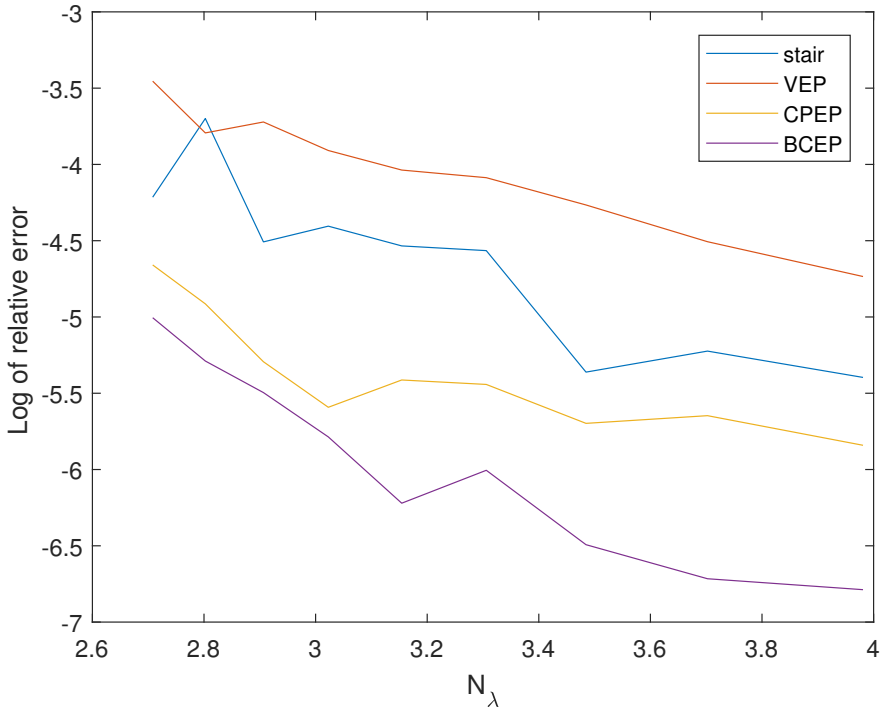

Figure 4.9: The average relative error of a cylinder in log scale, $\epsilon = 6$ and radius $r = 150nm$. $N_\lambda = \log(\frac{150nm}{\Delta x})$.

4.3 Stability

In this section, we investigate the stability of our new algorithm since the stability of other methods have been demonstrated in the literature. In order to test the stability of the BC-EP algorithm, two different tests are conducted. Firstly, the algorithm has been run for 200,000 iterations under FDTD main loop which is long enough for the electric and magnetic waves completely leave the region as seen in Figure 4.10 and Figure 4.11. This process has been repeated for $\epsilon = 3, 6, 10, 30$ and for mesh size $\Delta x = 10nm, 7.3nm, 4.6nm$, and $2.8nm$. At every $2,000$ iterations, a calculation of the SCS for all 601 wavelengths is conducted. Then the average relative error between the calculated SCS at that iteration and the exact SCS over those wavelengths is calculated. We observe that the result are very similar for different ϵ and different Δx in the sense that the relative errors drop down to zero very quickly. This shows that there is no electromagnetic power left in the region and the fields return back to zero as excepted, meaning no late time instability even at very high contrast.

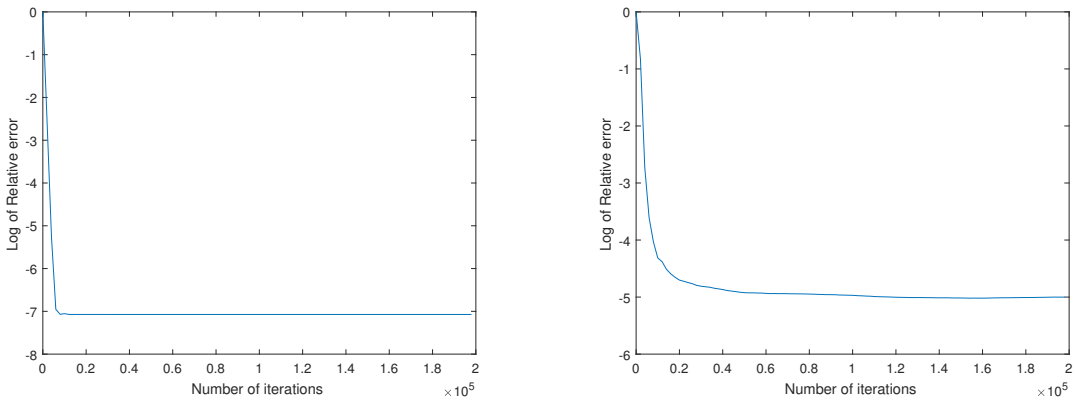

(a) $\epsilon = 3$ (b) $\epsilon = 10$

Figure 4.10: Relative error in log format for the SCS calculation at a given iteration for the cylinder with $r = 400nm$. $\Delta x = \Delta y = 4.6nm$.

For the second test, we run the algorithm and meanwhile keep track of the electric

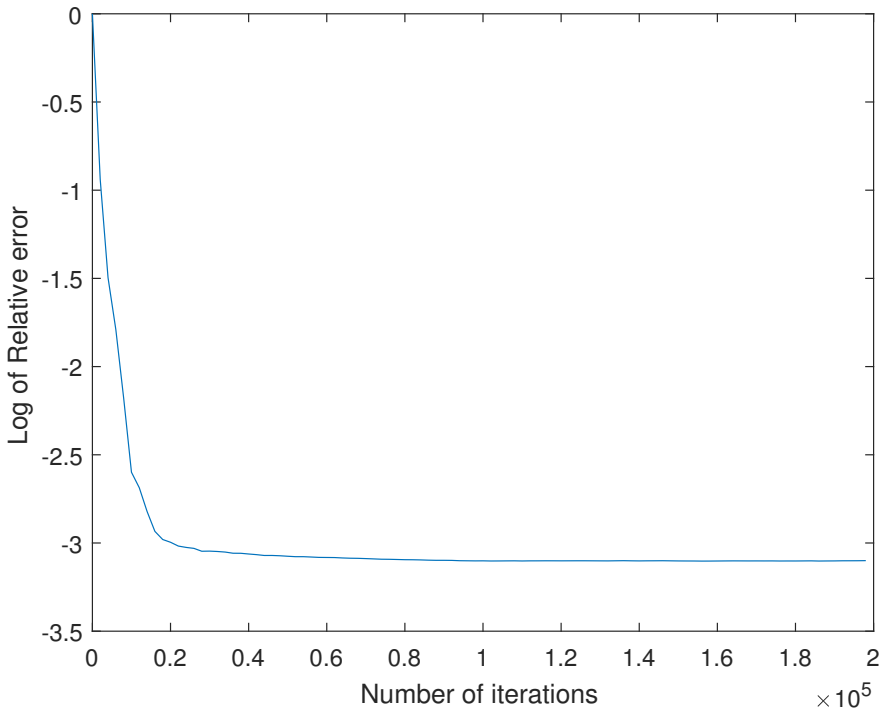

Figure 4.11: Relative error in log format for the SCS calculation at a given iteration for the cylinder with $r = 400nm$ and $\epsilon = 30$. $\Delta x = \Delta y = 4.6nm$.

and magnetic fields to assure that they go to zero as well. To this end, the field values are recorded at every 500 iterations. As seen in Figure 4.12, all the electric and magnetic fields go to zero quickly with time going on. It gives another strong evidence that no numerical artifacts are generated to cause instability.

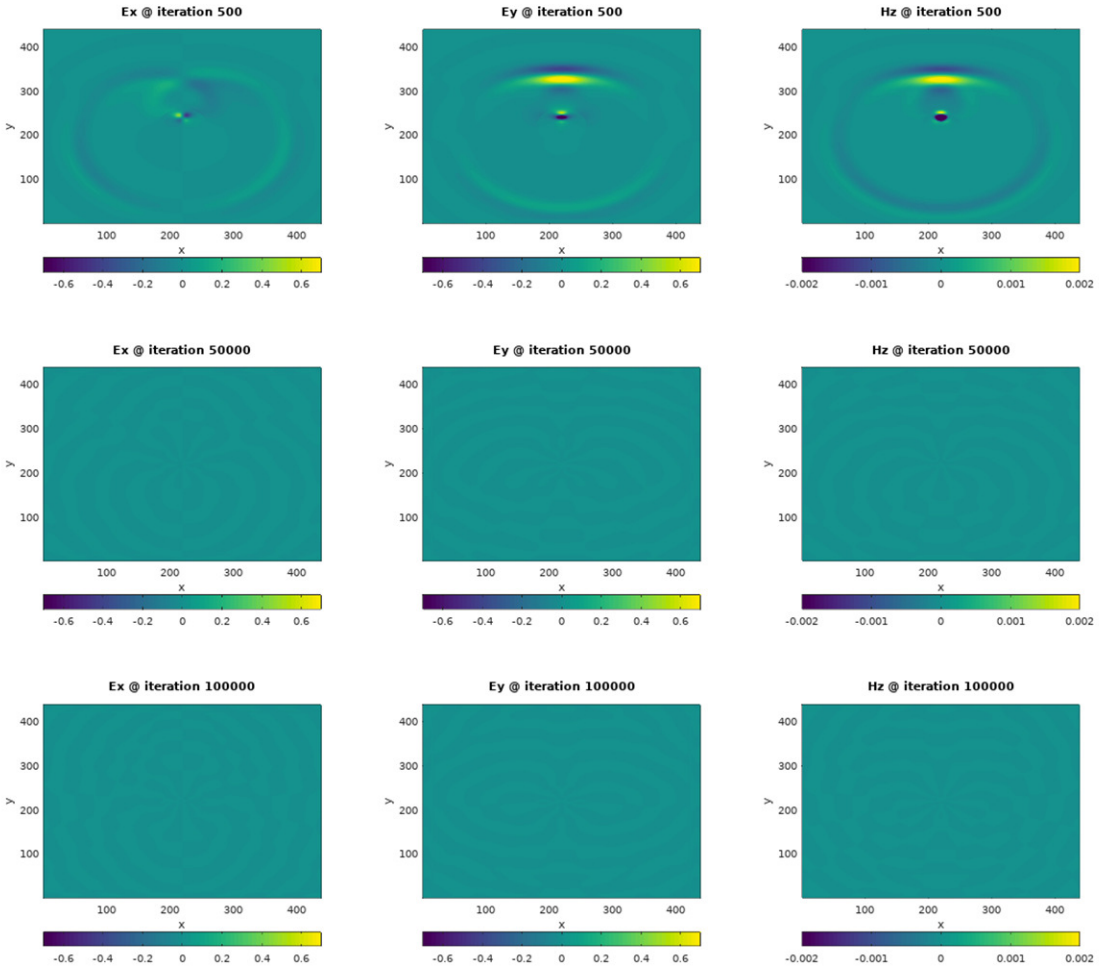

Figure 4.12: Field values at the stated iterations for the BC-EP implementation with $\epsilon = 6$ and $\Delta x = 10nm$.

Chapter 5

Conclusions and Future Reseach

In this final chapter, we will draw conclusions based on the previous chapters. Then we will briefly discuss the plan for future research.

Chapter 1 went through the background of basic FDTD methods to solve the Maxwell's equations. Chapter 2 covered all related numerical methods to solve Maxwell's equations to overcome the pixelation issue around the interface among multiple media.

In Chapter 3, we built our new BC-EP algorithm for the challenging transverse electric case where the tangential component of the electric field, the normal component of the electric displacement and the magnetic field are continuous across the interface between two different media. We set up a relation for the electric fields (as well as the electric displacement) on the different sides of the interface. Based on this important relationship and the integral version of the Maxwell's equations, we derived our new FDTD algorithm which represents Maxwell's equations accurately while the previous numerical methods skipped some terms from the boundary conditions for the purpose of algorithm simplification. We then proved that our new algorithm can reach second-order convergence $\mathcal{O}(\Delta x^2)$ with mesh size $\Delta x = \Delta y$ for any orientation of the interface between different media.

In Chapter 4, we considered a numerical example of a dielectric cylinder. We computed its total scattered cross section based on our new BC-EP algorithm and

compare our result with the analytic solution and the old results from those related numerical methods using effective permittivities reported in the literature. We considered two different radius of the cylinder: $r = 400nm$ and $r = 150nm$. The numerical results clearly demonstrated that our algorithm always achieves the highest convergence (close to second order) compared with all those methods. In order to demonstrate the stability of our new method, we ran the algorithm for a long time with high contrast of electric permittivities and found that both the electric and magnetic fields converge to zero very quickly and the total scattered cross section calculation was indeed stabilized. Therefore, our algorithm has been shown to be the most effective FDTD method to solve Maxwell's equations involving multiple media.

Currently, our new algorithm is very robust for multiple media with constant permittivities. Our next research consideration is to develop a new method based on our current one to handle more complicated dispersive materials whose permittivities are complex functions of light frequencies. Another possible research direction is to extend our algorithm to more general 3D transverse electric problems where both electric field $\mathbf{E}(x, y, z)$ and magnetic field $\mathbf{H}(x, y, z)$ are functions of all spatial variables x, y, z. The extensions of our current method to these two new scenarios are not straightforward and need further investigation and development of associated new algorithms.

References

[1] Carl a. Bauer, Gregory R. Werner, and John R. Cary. A second-order 3D electromagnetics algorithm for curved interfaces between anisotropic dielectrics on a Yee mesh. *Journal of Computational Physics*, 230(5):2060–2075, mar 2011. 18

[2] Jean-Pierre Berenger. A prefectly Matched Layer for the Absorption of Electromagntiec Waves. *Journal of Computational Physics*, 144:185–200, 1994. 1

[3] Craig F Bohren and Donald R. Huffman. *Absorption and scattering of light by small particles*. Wily-Interscience Publication, New York, 1983. 45, 46

[4] I.J. Craddock C.J. Railton and J.B. Schneider IC. Improved locally distorted CPFDTD algorithm with provable stability. *IEEE Transactions on Microwave Theory and Techniques*, 31(18):1585–1586, 1995. 13, 14

[5] Supriyo Dey and Raj Mittra. A conformal finite-difference time-domain technique for modeling cylindrical dielectric resonators. *IEEE Transactions on Microwave Theory and Techniques*, 47(9 PART 1):1737–1739, 1999. vi, 16

[6] a Farjadpour, David Roundy, Alejandro Rodriguez, M Ibanescu, Peter Bermel, J D Joannopoulos, Steven G Johnson, and G W Burr. Improving accuracy by subpixel smoothing in the finite-difference time domain. *Optics letters*, 31(20):2972–2974, 2006. vi, 17, 18

[7] Paul H. Harms and Jin Fa Lee. A Study of the Nonorthogonal FDTD Method Versus the Conventional FDTD Technique for Computing Resonant Frequencies of Cylindrical Cavities. *IEEE Transactions on Microwave Theory and Techniques*, 40(4):741–746, 1992. vi, 13

[8] T Hirono, Y Shibata, W W Lui, S Seki, Senior Member, and Y Yoshikuni. The Second-Order Condition for the Dielectric Interface Orthogonal to the Yee-Lattice Axis in the FDTD Scheme. *IEEE Mircoewave and Guided Wave Letters*, 10(9):359–361, 2000. 22

[9] Takuo Hirono, Yuzo Yoshikuni, and Takayuki Yamanaka. Effective permittivities with exact second-order accuracy at inclined dielectric interface for the two-dimensional finite-difference time-domain method. *Applied optics*, 49(7):1080–1096, 2010. 22

[10] Kyu-pyung Hwang, Student Member, and Andreas C Cangellaris. Effective Permittivities for Second-Order Accurate FDTD Equations at Dielectric Interfaces. *IEEE Mircowave and Wireless Components Letters*, 11(4):158–160, 2001. vii, 20, 40, 42, 43, 44

[11] Steven G. Johnson, M. Ibanescu, M. a. Skorobogatiy, O. Weisberg, J. D. Joannopoulos, and Y. Fink. Perturbation theory for Maxwell's equations with shifting material boundaries. *Physical Review E - Statistical, Nonlinear, and Soft Matter Physics*, 65(6):066611, jun 2002. 17

[12] Tg Jurgens, Allen Taflove, K. Umashankar, and T.G. Moore. Finite-difference time-domain modeling of curved surfaces (EM scattering). *IEEE Transactions on Antennas and Propagation*, 40(4):357–366, 1992. vi, 14, 15

[13] Chris Kottke, Ardavan Farjadpour, and Steven G. Johnson. Perturbation theory for anisotropic dielectric interfaces, and application to subpixel smoothing of discretized numerical methods. *Physical Review E - Statistical, Nonlinear, and Soft Matter Physics*, 77(3):036611, mar 2008. 17

[14] Lukasz Kulas and Michal Mrozowski. Reciprocity principle for stable subgridding in the finite difference time domain method. *EUROCON 2007 - The International Conference on Computer as a Tool*, pages 106–111, 2007. vi, 13, 14

[15] Xuefeng Liu, Numan Gozubenli, Baeck Choi, Peng Jiang, Timothy Meagher, and Bin Jiang. Templated Fabrication of Periodic Arrays of Metallic and Silicon Nanorings with Complex Nanostructures. *Nanotechnology*, page 055603, 2015. 23

[16] Jia Lu and Huaichun Zhou. Finite-difference time-domain modeling of curved material interfaces by using boundary condition equations method. *Chinese Physics B*, 25(9):090203, 2016. 22

[17] Ahmad Mohammadi, Hamid Nadgaran, and Mario Agio. Contour-path effective permittivities for the two-dimensional finite-difference time-domain method. *Optics express*, 13(25):76–89, 2005. vi, vii, 12, 21, 22, 45, 49

[18] Ardavan F Oskooi, Chris Kottke, and Steven G Johnson. of anisotropic media by subpixel smoothing. *Optics letters*, 34(18):2778–2780, 2009. 17

[19] Raymond C. Rumpf. Electromagnetic Analysis Using Finite-Difference Time-Domain. http://emlab.utep.edu/ee5390fdtd.htm, 2016. Accessed: 2018-01-22. vi, 6, 9

[20] Allen Taflove and Susan C. Hagness. *Computational Electrodynamics Finite - Difference Time-Domain*. Artech House, Boston, second edition, 2000. 2, 47

[21] Gregory R. Werner, Carl a. Bauer, and John R. Cary. A more accurate, stable, FDTD algorithm for electromagnetics in anisotropic dielectrics. *Journal of Computational Physics*, 255:436–455, dec 2013. vii, 12, 18, 19

[22] Gregory R. Werner and John R. Cary. A stable FDTD algorithm for non-diagonal, anisotropic dielectrics. *Journal of Computational Physics*, 226(1):1085–1101, sep 2007. vi, 17, 18

[23] Kane S Yee. Numerical Solution. *IEEE Transactions on Antennas and Propagation*, 14(3):302–307, 1966. 1, 4, 11